Research Square

Preprints are preliminary reports that have not undergone peer review.
They should not be considered conclusive, used to inform clinical practice,
or referenced by the media as validated information.

Legendre-Galerkin Chebyshev-collocation BDF method for longtime simulation of multidimensional wave equations on complex geometries

Qiancheng Tan

Guilin University of Electronic Technology https://orcid.org/0009-0007-7727-8640

Yonghui Qin

yonghui1676@163.com

Guilin University of Electronic Technology

Research Article

Keywords: LegendreGalerkin, Chebyshev collocation, wave equations

Posted Date: November 12th, 2026

DOI: https://doi.org/10.21203/rs.3.rs-11696959/v1

License: This work is licensed under a Creative Commons Attribution 4.0 International License.
Read Full License

Additional Declarations: The authors declare no competing interests.

Legendre-Galerkin Chebyshev-collocation BDF method for longtime simulation of multidimensional wave equations on complex geometries*

Qiancheng Tan[a], Yonghui Qin[a,b,c,*]

[a] College of Mathematics and Computing Science, Guangxi Colleges and Universities Key Laboratory of Data Analysis and Computation, Guilin University of Electronic Technology, Guilin 541004, China;
[b] Center for Applied Mathematics of Guangxi, Guilin University of Electronic Technology, Guilin 541004, China;
[c] Guangxi Key Laboratory of Automatic Detecting Technology and Instruments, Guilin University of Electronic Technology, Guilin 541004, China;

Abstract

This paper develops a LegendreGalerkin Chebyshevcollocation backward differentiation formula (LCCBDF6) for longtime simulations of multidimensional linear wave equations. The spatial discretization adopts LegendreGalerkin formulation combined with Chebyshev collocation at GaussLobatto points, while the sixthorder BDF method is used for time integration. A sequential loworder BDF starting procedure is presented to initialize the sixstep multistep scheme. Conditional stability and optimal convergence estimates are derived, showing the scheme achieves $O(\tau^6 + N^{1-\sigma})$ accuracy. By coordinate mapping and algebraic regularization for coordinate singularities, the method is extended to complex curved domains including disks, spheres and starshaped geometries. Numerical tests from one to threedimensional cases demonstrate that the pointwise L^∞ and RMS errors can be maintained at the 10^{-9} magnitude for curveddomain problems, confirming the spectral accuracy and favorable longtime behaviour of the proposed scheme.

Keywords: LegendreGalerkin, Chebyshev collocation, wave equations

1. Introduction

Spectral and pseudospectral methods are widely recognized for solving wave equations due to their high-order accuracy and exponential convergence rates for smooth solutions [12, 18]. However, conventional spectral methods are predominantly limited to simple, tensor-product domains [5, 19].

When applied to complex or non-rectangular geometriessuch as circular disks, spherical surfaces, or star-shaped/flower-like domainsstandard spectral discretizations face severe challenges, including polar singularities, boundary-fitting difficulties, and geometric mapping distortions [4, 10]. Furthermore, simulating wave propagation over long time intervals often suffers from accumulated numerical dispersion and dissipation errors, leading to severe accuracy degradation in traditional time-stepping schemes [3, 14]. Although various domain decomposition and mapped spectral methods have been developed [15, 17], simultaneously achieving long-time high precision and spectral boundary-fitting flexibility across one- to three-dimensional complex geometries remains a major computational challenge [11].

In this paper, we consider the following initial-boundary value problem for the linear wave equation in a d-dimensional bounded domain $\Omega \subset \mathbb{R}^d$ $(d = 1, 2, 3)$ as

*This work is supported by the National Natural Science Foundation of China (No.12026265,12026266) and Guangxi Key Laboratory of Automatic Detecting Technology and Instruments (No. YQ22106).

Email address: yonghui1676@163.com (Yonghui Qin)
[1]Corresponding author. (Y. Qin)

$$\begin{cases} \dfrac{\partial^2 u}{\partial t^2} - \alpha^2 \Delta u = f(\boldsymbol{x}, t), & \boldsymbol{x} \in \Omega,\ t \in (0, T], \\ u|_{\partial\Omega} = 0, & t \in [0, T], \\ u(\boldsymbol{x}, 0) = u_0(\boldsymbol{x}), & \boldsymbol{x} \in \Omega, \\ \dfrac{\partial u}{\partial t}(\boldsymbol{x}, 0) = u_1(\boldsymbol{x}), & \boldsymbol{x} \in \Omega, \end{cases} \tag{1.1}$$

where $\alpha > 0$ denotes the wave speed, and $u_0(\boldsymbol{x})$ and $u_1(\boldsymbol{x})$ are the prescribed initial displacement and initial velocity, respectively.The LegendreChebyshev collocation BFD6 (LCC-BFD6) method is developed to solve the problem (1.1). The scheme is based on the Legendre and Chebyshev pseudospectral collocation methods, where the spatial derivatives are discretized at the corresponding GaussLobatto collocation points. The sixth-order backward differentiation formula (BFD6) is employed for the time discretization. The scheme preserves long-time high precision and robust numerical stability. By introducing appropriate coordinate mappings, the proposed method is extended to deal with complex curved geometries, including circular disks and spherical domains. The stability and the optimal rate of convergence are derived. Applications of the LCC-BFD6 method to one- to three-dimensional wave equations on rectangular, circular, and spherical domains are considered.

The article is organized as follows. In Section 2 we introduce the notation and formulate the fully discrete scheme, combining the spatial spectral discretization with the BDF6 time integrator, and we describe the startup procedure for the six-step formula. Section 3 collects the approximation results used in the analysis. In Section 4 the stability of the fully discrete scheme is characterized and the optimal convergence rates are derived. Section 5 discusses the implementation on circular and spherical domains. Section 6 presents numerical experiments in tensor-product, circular and spherical domains that illustrate the accuracy, the stability restriction and the long-time behaviour of the method. Concluding remarks are given in Section 7.

2. Notations and schemes

In this section, we present some necessary notation and formulate the LCC-BFD6 scheme. Let $(\cdot,\cdot)_J$ and $\|\cdot\|_J$ denote the inner product and norm in $L^2(J)$, respectively. For any integer $\sigma \geq 0$, we adopt standard notation $H^\sigma(J)$ to represent the Sobolev space equipped with norm $\|\cdot\|_{\sigma,J}$ and semi-norm $|\cdot|_{\sigma,J}$. When the domain of integration is I, the subscript J is omitted. Let $H_0^1(I) = \{u \in H^1(I) : u(-1) = u(1) = 0\}$ denote the Sobolev subspace with homogeneous Dirichlet boundary conditions, and $H^{-1}(I) = (H_0^1(I))'$ denote its dual space. Let $\hat{x}_j$ be the Chebyshev–Gauss–Lobatto (CGL) nodes on the reference interval $\hat{I} = (-1, 1)$. The physical grid point set on I is given by

$$I_N = \{x_j : x_j = \hat{x}_j,\ 0 \leq j \leq N\}. \tag{2.1}$$

In this paper, standard Sobolev spaces on the single interval I will be utilized. We consider functions $u \in H^\sigma(I)$ and define the associated semi-norm

$$|u|_{\sigma,I} = |u|_\sigma. \tag{2.2}$$

When the domain of integration is Ω, the subscript for inner products and norms is omitted.

Let $\mathbb{P}_{N_i}$ denote the space of univariate polynomials of degree at most N_i along the i-th coordinate direction. We define the tensor-product polynomial spaces as

$$\begin{aligned} \mathbb{P}_N(\Omega) &= \left\{\varphi \in H^1(\Omega) : \varphi \in \mathbb{P}_{N_i} \text{ in the } i\text{-th direction},\ i = 1, 2, \ldots, d\right\}, \\ V_N &= \left\{\varphi \in H_0^1(\Omega) : \varphi \in \mathbb{P}_{N_i} \text{ in the } i\text{-th direction},\ i = 1, 2, \ldots, d\right\}. \end{aligned} \tag{2.3}$$

By introducing the velocity variable $v = \partial_t u$, the original second-order wave problem (1.1) can be reduced to a first-order system in time. Its weak formulation is to find $u(t) \in H_0^1(\Omega)$ and $v(t) \in L^2(\Omega)$ such that for

any test functions $p \in L^2(\Omega)$ and $q \in H_0^1(\Omega)$, there holds

$$\begin{cases} (\partial_t u, p) - (v, p) = 0, & t > 0, \\ (\partial_t v, q) + \alpha^2 (\nabla u, \nabla q) = (f, q), & t > 0, \\ u(\boldsymbol{x}, 0) = u_0(\boldsymbol{x}), \quad v(\boldsymbol{x}, 0) = u_1(\boldsymbol{x}), & \boldsymbol{x} \in \Omega, \end{cases} \tag{2.4}$$

where the homogeneous Dirichlet boundary condition is essentially satisfied by the trial and test function spaces.

We define the multi-dimensional discrete polynomial spaces as

$$U_N = \left\{ u \in H_0^1(\Omega) : u \in \mathbb{P}_N(\Omega) \right\}, \quad V_N = \left\{ v \in L^2(\Omega) : v \in \mathbb{P}_N(\Omega) \right\}. \tag{2.5}$$

The semi-discrete Legendre–Galerkin Chebyshev collocation approximation is to find $(u_N, v_N) \in U_N \times V_N$ such that for any $p \in V_N$ and $q \in U_N$, it satisfies

$$\begin{cases} (\partial_t u_N, p) - (v_N, p) = 0, & t > 0, \\ (\partial_t v_N, q) + \alpha^2 (\nabla u_N, \nabla q) = (I_N^C f, q), & t > 0, \\ u_N(\boldsymbol{x}, 0) = I_N^C u_0(\boldsymbol{x}), \quad v_N(\boldsymbol{x}, 0) = I_N^C u_1(\boldsymbol{x}), & \boldsymbol{x} \in \Omega. \end{cases} \tag{2.6}$$

Here, the operator I_N^C represents the multi-dimensional tensor-product Chebyshev interpolation operator, satisfying the interpolation condition at the tensor-product grids:

$$(I_N^C v)(\boldsymbol{x_j}) = v(\boldsymbol{x_j}), \quad \text{with } \boldsymbol{x_j} = (x_{j_1}^1, \ldots, x_{j_d}^d),\ x_{j_i}^i \in I_N^i,\ 0 \le j_i \le N_i,\ i = 1, 2, \ldots, d. \tag{2.7}$$

To derive the matrix representation, let $\hat{\boldsymbol{u}}$ and $\hat{\boldsymbol{v}}$ be the corresponding coefficient vectors of the numerical solutions. The semi-discrete scheme can be rewritten in the following algebraic matrix form:

$$\begin{cases} M \partial_t \hat{\boldsymbol{u}} - M \hat{\boldsymbol{v}} &= \boldsymbol{0}, \\ \partial_t \hat{\boldsymbol{v}} + \alpha^2 M^{-1} S \hat{\boldsymbol{u}} &= M^{-1} \boldsymbol{g}, \end{cases} \tag{2.8}$$

where M and S are the multi-dimensional mass and stiffness matrices, respectively. Letting $\boldsymbol{U} = (\hat{\boldsymbol{u}}^T, \hat{\boldsymbol{v}}^T)^T$ be the concatenated vector, the above system can be cast into a block matrix form as

$$\begin{pmatrix} \partial_t \hat{\boldsymbol{u}} \\ \partial_t \hat{\boldsymbol{v}} \end{pmatrix} + \begin{bmatrix} 0 & -I \\ \alpha^2 M^{-1} S & 0 \end{bmatrix} \begin{pmatrix} \hat{\boldsymbol{u}} \\ \hat{\boldsymbol{v}} \end{pmatrix} = \begin{pmatrix} \boldsymbol{0} \\ M^{-1} \boldsymbol{g} \end{pmatrix}, \tag{2.9}$$

which is compactly written as

$$\partial_t \boldsymbol{U} + A \boldsymbol{U} = \boldsymbol{G}. \tag{2.10}$$

Let τ be the time step size and define $t_k = k\tau$ for $k = 0, 1, \ldots, n_T$, where $n_T \tau = T$. We denote the variables at time t_k as

$$u_N^k := u_N(t_k), \qquad v_N^k := v_N(t_k). \tag{2.11}$$

For the first-order system (2.6), the s-step backward differentiation formula (BDF, $s = 1, 2, \ldots, 6$) is employed for the time discretization. The BDF discrete time derivative is defined as

$$\delta_\tau \varphi^{k+1} = \frac{1}{\tau} \sum_{i=0}^{s} \alpha_{s,i} \varphi^{k+1-i}. \tag{2.12}$$

Consequently, the fully discrete scheme is to find $u_N^{k+1} \in U_N$ and $v_N^{k+1} \in V_N$ such that for any $p \in V_N$ and $q \in U_N$, there holds

$$\begin{cases} \left(\delta_\tau u_N^{k+1}, p\right) - \left(v_N^{k+1}, p\right) = 0, \\ \left(\delta_\tau v_N^{k+1}, q\right) + \alpha^2 \left(\nabla u_N^{k+1}, \nabla q\right) = \left(I_N^C f^{k+1}, q\right), \end{cases} \tag{2.13}$$

where the BDF coefficients $\{\alpha_{s,i}\}$ are given by

$$\alpha_{s,0} = \sum_{j=1}^{s} \frac{1}{j}, \qquad \alpha_{s,i} = \frac{(-1)^i}{i} \binom{s}{i}, \quad i = 1, 2, \ldots, s. \tag{2.14}$$

These coefficients satisfy the following consistency conditions:

$$\sum_{i=0}^{s} \alpha_{s,i} = 0, \qquad \sum_{i=0}^{s} i\, \alpha_{s,i} = -1, \tag{2.15}$$

which guarantee that the time discretization attains an s-th order accuracy. The specific values of the coefficients for $s = 1, \ldots, 6$ are summarized in Table 1.

Table 1: The coefficients $\alpha_{s,i}$ for the s-step BDF schemes.

s	$\alpha_{s,0}$	$\alpha_{s,1}$	$\alpha_{s,2}$	$\alpha_{s,3}$	$\alpha_{s,4}$	$\alpha_{s,5}$	$\alpha_{s,6}$
1	1	-1					
2	$\frac{3}{2}$	-2	$\frac{1}{2}$				
3	$\frac{11}{6}$	-3	$\frac{3}{2}$	$-\frac{1}{3}$			
4	$\frac{25}{12}$	-4	3	$-\frac{4}{3}$	$\frac{1}{4}$		
5	$\frac{137}{60}$	-5	5	$-\frac{10}{3}$	$\frac{5}{4}$	$-\frac{1}{5}$	
6	$\frac{49}{20}$	-6	$\frac{15}{2}$	$-\frac{20}{3}$	$\frac{15}{4}$	$-\frac{6}{5}$	$\frac{1}{6}$

By expanding the BDF time derivative and moving all historical terms to the right-hand side, (2.13) can be reformulated as the one-step iteration:

$$\begin{cases} \dfrac{\alpha_{s,0}}{\tau} \left(u_N^{k+1}, p\right) - \left(v_N^{k+1}, p\right) = -\dfrac{1}{\tau} \displaystyle\sum_{i=1}^{s} \alpha_{s,i} \left(u_N^{k+1-i}, p\right), \\ \dfrac{\alpha_{s,0}}{\tau} \left(v_N^{k+1}, q\right) + \alpha^2 \left(\nabla u_N^{k+1}, \nabla q\right) = \left(I_N^C f^{k+1}, q\right) - \dfrac{1}{\tau} \displaystyle\sum_{i=1}^{s} \alpha_{s,i} \left(v_N^{k+1-i}, q\right). \end{cases} \tag{2.16}$$

In block matrix form, letting $\boldsymbol{U}^{k+1} = (\hat{\boldsymbol{u}}^{k+1}, \hat{\boldsymbol{v}}^{k+1})^T$, we obtain the fully discrete algebraic system

$$\frac{\alpha_{s,0}}{\tau} \boldsymbol{U}^{k+1} + A\boldsymbol{U}^{k+1} = \boldsymbol{r}^k, \tag{2.17}$$

where the right-hand side vector containing historical information is given by

$$\boldsymbol{r}^k = -\frac{1}{\tau} \sum_{i=1}^{s} \alpha_{s,i} \boldsymbol{U}^{k+1-i} + \boldsymbol{F}^{k+1}, \tag{2.18}$$

with $\boldsymbol{F}^{k+1} = (\boldsymbol{0}^T, (I_N^C f^{k+1})^T)^T$ and the block matrix $A = \begin{bmatrix} 0 & -I \\ \alpha^2 M^{-1} S & 0 \end{bmatrix}$.

Here, the entries of the multi-dimensional mass matrix M and stiffness matrix $K = \alpha^2 S$ are computed by

$$M_{ij} = (\phi_i, \phi_j)_\Omega, \qquad K_{ij} = \alpha^2 S_{ij} = \alpha^2 (\nabla \phi_i, \nabla \phi_j)_\Omega, \tag{2.19}$$

where $\{\phi_i\}$ denotes a set of multi-dimensional tensor-product basis functions for the space U_N. The algebraic system (2.16) can be solved directly to update u_N^{k+1} and v_N^{k+1} simultaneously, without the need to eliminate the velocity variable v_N^{k+1} in advance.

3. Preliminaries

Some results for approximation are presented. First, the coordinate relations between the physical domain $\Omega = \prod_{i=1}^{d}(a_i, b_i)$ and the reference domain $\hat{\Omega} = (-1, 1)^d$ are given as follows:

$$x_i = \frac{h_i \hat{x}_i + a_{i-1} + a_i}{2}, \quad \hat{x}_i \in (-1, 1), \quad i = 1, 2, \ldots, d, \tag{3.1}$$

where $h_i = a_i - a_{i-1}$ is the length of the interval in the i-th direction.

Let $\hat{P}^1_{N_i} : H^1(-1, 1) \to \mathbb{P}_{N_i}$ be the one-dimensional H^1-projection operator on the reference element, defined as

$$\hat{P}^1_{N_i}\hat{\varphi}(\hat{x}) = \hat{\varphi}(-1) + \int_{-1}^{\hat{x}} \hat{P}_{N_i-1}\partial_y\hat{\varphi}(y)\mathrm{d}y, \tag{3.2}$$

where $\hat{P}_{N_i} : L^2(-1, 1) \to \mathbb{P}_{N_i}$ is the standard L^2-orthogonal projection operator. We generate the multi-dimensional H^1-projection operator $P^1_N : H^1(\Omega) \to \mathbb{P}_N(\Omega)$ via the tensor product of the 1D operators such that

$$(P^1_N\varphi)(\boldsymbol{x}) = \left(P^{1,x_1}_{N_1} \otimes \cdots \otimes P^{1,x_d}_{N_d}\right)\varphi(\boldsymbol{x}). \tag{3.3}$$

Similarly, the multi-dimensional Chebyshev interpolation operator is defined as $I^C_N = I^{C,x_1}_{N_1} \otimes \cdots \otimes I^{C,x_d}_{N_d}$.

We set $N = \min_{1\le i\le d} N_i$, and present the following approximation results. Let C be a generic positive constant independent of h_i, N_i, the time step τ, and any function.

Lemma 1. *If $\varphi \in H^\sigma(\Omega)$ for $\sigma \ge 1$ and $0 \le r \le 1$, then*

$$\|P^1_N\varphi - \varphi\|_{H^r(\Omega)} \le CN^{r-\sigma}\|\varphi\|_{H^\sigma(\Omega)}. \tag{3.4}$$

Lemma 2. *If $\varphi \in H^\sigma(\Omega)$ for $\sigma > d/2$ and $0 \le r \le 1$, then*

$$\|I^C_N\varphi - \varphi\|_{H^r(\Omega)} \le CN^{r-\sigma}\|\varphi\|_{H^\sigma(\Omega)}. \tag{3.5}$$

To facilitate the convergence analysis of the fully discrete scheme, the following inverse inequality for polynomials and the discrete Gronwall's lemma are required.

Lemma 3. *For any polynomial $\varphi \in \mathbb{P}_N(\Omega)$, there exists a positive constant C such that*

$$\|\nabla\varphi\|_{L^2(\Omega)} \le CN^2\|\varphi\|_{L^2(\Omega)}. \tag{3.6}$$

Lemma 4 (Discrete Gronwall's Lemma)**.** *Let $\tau > 0$ and $B \ge 0$. Let a_k, b_k, c_k, γ_k be non-negative sequences such that*

$$a_n + \tau\sum_{k=0}^{n} b_k \le \tau\sum_{k=0}^{n}\gamma_k a_k + \tau\sum_{k=0}^{n} c_k + B \quad \text{for } n \ge 0. \tag{3.7}$$

Suppose $\tau\gamma_k < 1$ for all k. Then there exists a constant C^* depending only on γ_k such that

$$a_n + \tau\sum_{k=0}^{n} b_k \le C^*\left(\tau\sum_{k=0}^{n} c_k + B\right). \tag{3.8}$$

4. LCC-BFD6 method for the wave equation problem

In this section we analyse the stability of the fully discrete LCC-BDF6 scheme (2.13) and derive its convergence rate. A simple discrete energy inequality of the form $2(\delta_\tau\varphi^{k+1}, \varphi^{k+1}) \ge \tau^{-1}\big(\|\varphi^{k+1}\|^2 - \|\varphi^k\|^2\big)$, employed in an earlier draft of this work holds only for one-step time integrators and fails for $s \ge 2$. We therefore establish stability via modal analysis, which further yields the step-size constraint of the scheme.

4.1. Stability analysis

Assume that (u_N^k, v_N^k) and the right-hand term of (2.13) admit error perturbations $(\tilde{u}_N^k, \tilde{v}_N^k) \in U_N \times V_N$ and $\tilde{f}^k$, respectively. For any test functions $p \in V_N$ and $q \in U_N$, with $0 \le k \le n_T - 1$, the error perturbation equations read

$$\begin{cases} (\delta_\tau \tilde{u}_N^{k+1}, p) - (\tilde{v}_N^{k+1}, p) = 0, \\ (\delta_\tau \tilde{v}_N^{k+1}, q) + \alpha^2 (\nabla \tilde{u}_N^{k+1}, \nabla q) = (I_N^C \tilde{f}^{k+1}, q). \end{cases} \tag{4.1}$$

Substituting $p = \alpha^2 \tilde{u}_N^{k+1}$ and $q = \tilde{v}_N^{k+1}$ into (4.1), and using the relation $\tilde{v}_N^{k+1} = \delta_\tau \tilde{u}_N^{k+1}$, we rewrite the perturbation system in compact form:

$$\delta_\tau \tilde{\boldsymbol{U}}^{k+1} + A \tilde{\boldsymbol{U}}^{k+1} = \tilde{\boldsymbol{G}}^{k+1}, \tag{4.2}$$

where $\tilde{\boldsymbol{U}} = (\tilde{u}_N, \tilde{v}_N)^T$, the constant block operator A is defined in (2.9), and $\tilde{\boldsymbol{G}}$ collects the perturbation of the right-hand side.

Consider the generalized eigenvalue problem for the spatial discretization:

$$S \boldsymbol{\phi}_j = \lambda_j M \boldsymbol{\phi}_j, \quad j = 1, 2, \dots, M. \tag{4.3}$$

Since M and S are symmetric positive definite, there exist positive real eigenvalues $0 < \lambda_1 \le \lambda_2 \le \cdots \le \lambda_{\max}$ and a complete set of M-orthogonal eigenvectors satisfying $(\boldsymbol{\phi}_i, M\boldsymbol{\phi}_j) = \delta_{ij}$. Accordingly, the spectrum of A is purely imaginary:

$$\sigma(A) = \left\{ \pm \mathrm{i}\alpha \sqrt{\lambda_j} \right\}_{j=1}^{M}. \tag{4.4}$$

Expand the perturbation quantities in this eigenbasis:

$$\tilde{\boldsymbol{U}}^k = \sum_{j=1}^{M} w_j^k \boldsymbol{\phi}_j, \quad \tilde{\boldsymbol{G}}^k = \sum_{j=1}^{M} \tilde{g}_j^k \boldsymbol{\phi}_j. \tag{4.5}$$

Substituting (4.5) into (4.2) and invoking M-orthogonality, the system decouples into independent scalar s-step BDF recursions:

$$\delta_\tau w_j^{k+1} + \mathrm{i}\alpha \sqrt{\lambda_j}\, w_j^{k+1} = \tilde{g}_j^{k+1}, \qquad j = 1, 2, \dots, M, \tag{4.6}$$

which is exactly the s-step BDF discretization of the model ODE $w' = \mathrm{i}\alpha \sqrt{\lambda_j}\, w$.

Let $z_j = \mathrm{i}\alpha\tau \sqrt{\lambda_j}$. The recursion (4.6) is stable if and only if all roots of the characteristic polynomial

$$\rho(\zeta; z_j) = (\alpha_{s,0} + z_j)\zeta^s + \alpha_{s,1}\zeta^{s-1} + \cdots + \alpha_{s,s} = 0 \tag{4.7}$$

lie in the closed unit disk, with only simple roots on the unit circle. This root condition is equivalent to

$$z_j \in \mathcal{S}_s, \tag{4.8}$$

where $\mathcal{S}_s$ denotes the stability region of the s-step BDF method.

For $s \ge 3$, $\mathcal{S}_s$ reduces to an $A(\vartheta)$-sector $|\arg(-z)| \le \vartheta_s$ around the negative real axis, with the maximum angles ϑ_s given in [1]. Since the spectrum of the present problem is purely imaginary, we further determine the portions of the imaginary axis that lie outside $\mathcal{S}_s$ by solving the roots of (4.7) with $z = \mathrm{i}y$. The results are summarised in Table 2.

Table 2: Maximum $A(\vartheta)$-stability angles of s-step BDF formulas [1] and unstable intervals on the imaginary axis, computed from (4.7).

s	ϑ_s (degrees)	unstable range of $\lvert\mathrm{Im}\, z\rvert$
1	90.00	none
2	90.00	none
3	86.03	0 to 1.933
4	73.35	0 to 4.709
5	51.84	0.711 to 9.379
6	17.84	0.844 to 17.567

For the LegendreGalerkin discretization of the Laplacian, the maximum eigenvalue satisfies

$$\sqrt{\lambda_{\max}} \le C_\star N^2, \tag{4.9}$$

and in one dimension $\sqrt{\lambda_{\max}} \approx 0.167\, N^2$ for the polynomial degrees considered below. Combining (4.8) and (4.9), we impose the CFL-type step-size constraint

$$\tau\alpha\sqrt{\lambda_{\max}} \le \rho < \beta_6, \tag{4.10}$$

where $\beta_6 = 0.844$ is the first intersection of $\partial\mathcal{S}_6$ with the positive imaginary axis (see Table 2). Under this condition all scaled eigenvalues lie strictly inside $\mathcal{S}_s$, and we obtain the following conditional stability result.

Theorem 4.1 (Conditional stability)**.** *Let the time step τ satisfy (4.10). Then there exists a constant $C = C(\rho, s) > 0$, independent of N, τ and time index n, such that*

$$\|\tilde{\boldsymbol{U}}^n\|_M \le C\left(\|\tilde{\boldsymbol{U}}^0\|_M + \tau\sum_{k=0}^{n-1}\|\tilde{\boldsymbol{G}}^{k+1}\|_M\right), \qquad 0 \le n \le n_T, \tag{4.11}$$

where $\|\cdot\|_M$ denotes the norm induced by the mass matrix M.

Proof. For each mode j, rewrite (4.6) in companion matrix form:

$$\boldsymbol{w}_j^{k+1} = C(z_j)\boldsymbol{w}_j^k + \boldsymbol{b}\,\tilde{g}_j^{k+1}, \tag{4.12}$$

with $\boldsymbol{w}_j^k = (w_j^{k-s+1}, \dots, w_j^k)^T$ and $C(z_j)$ the $s\times s$ companion matrix associated with polynomial (4.7). Under condition (4.10), all eigenvalues of $C(z_j)$ lie strictly inside the unit disk, hence there exists $C_1 = C_1(\rho, s)$ such that

$$\|C(z_j)^n\| \le C_1, \quad \forall n \ge 0. \tag{4.13}$$

By the discrete variation-of-constants formula,

$$|w_j^n| \le C_1\left(|w_j^0| + \tau\sum_{k=0}^{n-1}|\tilde{g}_j^{k+1}|\right). \tag{4.14}$$

Summing over all modes and applying Parseval's identity for the M-orthogonal basis yields

$$\|\tilde{\boldsymbol{U}}^n\|_M^2 = \sum_{j=1}^{M}|w_j^n|^2 \le C_1^2\sum_{j=1}^{M}\left(|w_j^0| + \tau\sum_{k=0}^{n-1}|\tilde{g}_j^{k+1}|\right)^2. \tag{4.15}$$

Applying the CauchySchwarz inequality to the right-hand side and using norm equivalence completes the proof of (4.11). □

Remark 1. Estimate (4.11) is uniform with respect to the number of time steps, which is essential for long-time integration. The constant C degenerates as $\rho \to \beta_6^-$.

Remark 2. For $s = 1, 2$, the entire imaginary axis lies in $\mathcal{S}_s$, and G-stability theory yields unconditional stability, consistent with Dahlquist's order barrier for A-stable linear multistep methods. For $s \ge 3$, stability holds only under constraint (4.10).

Remark 3. For BDF6, $\mathcal{S}_6$ also contains the region $|\mathrm{Im}\, z| \ge 17.567$, giving a second disconnected stable interval. This interval has no practical value, as such large time steps resolve neither high-frequency modes nor the solution.

Remark 4. The scaling $\tau = O(N^{-2})$ is standard for Legendre spectral methods. A KosloffTal-Ezer mapping can relax this constraint to $\tau = O(N^{-1})$ at the cost of clustered grid points, which is a natural extension of the present scheme.

4.2. Convergence analysis

Next, we establish the optimal error estimates for the LCC-BDF6 method. Let $u(\boldsymbol{x},t)$ and $v(\boldsymbol{x},t) = \partial_t u(\boldsymbol{x},t)$ be the exact solutions to the wave equation problem. Define the projection approximations as $U_N^k = P_N^1 u(t_k)$ and $V_N^k = P_N^1 v(t_k)$. We decompose the numerical errors into

$$e_u^k = u_N^k - U_N^k \in U_N, \qquad e_v^k = v_N^k - V_N^k \in V_N. \tag{4.16}$$

The projection truncation equations can be formulated as

$$\begin{cases} (\delta_\tau U_N^{k+1}, p) - (V_N^{k+1}, p) = (G_u^{k+1}, p), \\ (\delta_\tau V_N^{k+1}, q) + \alpha^2(\nabla U_N^{k+1}, \nabla q) = (I_N^C f^{k+1} + G_v^{k+1}, q), \end{cases} \tag{4.17}$$

where $G_u^{k+1} = (\delta_\tau U_N^{k+1} - \partial_t u^{k+1}) + (v^{k+1} - V_N^{k+1})$, and G_v^{k+1} is decomposed into three distinct error components:

$$\begin{aligned} G_v^{k+1} &= (\partial_t v^{k+1} - \delta_\tau V_N^{k+1}) + \alpha^2(\nabla u^{k+1} - \nabla U_N^{k+1}) + (I_N^C f^{k+1} - f^{k+1}) \\ &=: G_{v,1}^{k+1} + G_{v,2}^{k+1} + G_{v,3}^{k+1}. \end{aligned} \tag{4.18}$$

Subtracting the projection equations from the fully discrete scheme (2.13), the error equations for (e_u^{k+1}, e_v^{k+1}) satisfy

$$\begin{cases} (\delta_\tau e_u^{k+1}, p) - (e_v^{k+1}, p) = (G_u^{k+1}, p), \\ (\delta_\tau e_v^{k+1}, q) + \alpha^2(\nabla e_u^{k+1}, \nabla q) = (G_v^{k+1}, q), \\ e_u^0 = I_N^C u_0 - P_N^1 u_0, \quad e_v^0 = I_N^C u_1 - P_N^1 u_1. \end{cases} \tag{4.19}$$

According to Theorem 4.1 and Lemmas 1–2, we estimate the terms in $\gamma^n(e_u, e_v, G_v)$ as follows:

$$\tau \sum_{k=0}^{n-1} \|G_{v,1}^{k+1}\|^2 \le C\tau^{12} \|\partial_t^7 v\|^2_{L^2(0,T;L^2(\Omega))}, \tag{4.20}$$

$$\tau \sum_{k=0}^{n-1} \|G_{v,2}^{k+1}\|^2 \le CN^{2(1-\sigma)} \|\nabla u\|^2_{L^2(0,T;H^\sigma(\Omega))} \le CN^{2(1-\sigma)} \|u\|^2_{L^2(0,T;H^{\sigma+1}(\Omega))}. \tag{4.21}$$

Furthermore, the Chebyshev interpolation error term is bounded by $\|G_{v,3}^{k+1}\| = \|I_N^C f^{k+1} - f^{k+1}\| \le CN^{-\sigma} \|f^{k+1}\|_{H^\sigma(\Omega)}$. For the initial errors, Lemmas 1 and 2 give

$$\|e_v^0\| + \alpha \|\nabla e_u^0\| = \|(I_N^C - P_N^1)u_1\|_{L^2(\Omega)} + \alpha \|\nabla (I_N^C - P_N^1) u_0\|_{L^2(\Omega)} \le CN^{1-\sigma}(\|u_0\|_{H^\sigma(\Omega)} + \|u_1\|_{H^\sigma(\Omega)}). \tag{4.22}$$

Applying Theorem 4.1 to the error system (4.19), for a sufficiently small time step τ independent of N, we obtain

$$B^n(e_u, e_v) \le C\gamma^n(e_u, e_v, G_v), \quad \forall n\tau \le T. \tag{4.23}$$

Taking square roots on both sides and combining with the triangle inequality $\|u(t_k) - u_N^k\|_{H^1(\Omega)} \le \|u(t_k) - U_N^k\|_{H^1(\Omega)} + \|e_u^k\|_{H^1(\Omega)}$, we arrive at the main convergence theorem.

Theorem 4.2 (Convergence)**.** *Let (u, v) and (u_N^k, v_N^k) denote the exact solution and the numerical solution of the LCC-BDF6 scheme (2.13), respectively. Assume that $\sigma > d/2$,*

$$u \in C\big([0,T]; H^{\sigma+1}(\Omega)\big), \qquad \partial_t^7 v \in L^2\big(0,T; L^2(\Omega)\big), \qquad f \in C\big([0,T]; H^\sigma(\Omega)\big), \tag{4.24}$$

that the data satisfy the compatibility conditions required for this regularity, and that the time step obeys (4.10) for some $0 < \rho < \beta_6$. Then there exists a constant C, independent of N, of τ and of the time level k but depending on T, ρ, α and σ, such that

$$\begin{aligned} \|u(t_k) - u_N^k\|_{H^1(\Omega)} &\le C\big(\tau^6 + N^{1-\sigma}\big), \\ \|\partial_t u(t_k) - v_N^k\|_{L^2(\Omega)} &\le C\big(\tau^6 + N^{1-\sigma}\big), \end{aligned} \qquad 0 \le k \le n_T. \tag{4.25}$$

Remark 5. The two estimates in (4.25) are stated separately because they hold in different norms. The dependence of C on T enters through the accumulation of the local errors for the finite-time bound in Theorem 4.2. In contrast with a standard Gronwall argument yielding an exponential factor e^{CT}, the stability estimate (4.11) is uniform in the number of time steps, which permits a rigorous long-time error analysis based on modulated Fourier expansions. Under the same regularity assumptions as in Theorem 4.2 together with the CFL condition (4.10), for all $t_k = k\tau \in [0, \infty)$, we obtain the long-time error bound

$$\|u(t_k) - u_N^k\|_{H^1(\Omega)} \leq C\left(\tau^6 + N^{1-\sigma}\right)(1 + t_k),$$
$$\|\partial_t u(t_k) - v_N^k\|_{L^2(\Omega)} \leq C\left(\tau^6 + N^{1-\sigma}\right)(1 + t_k),$$

where the constant $C > 0$ is independent of τ, N and t_k. This shows that the error grows at most linearly in time, which is dominated by the accumulation of phase error for oscillatory wave solutions [20]. Rigorous long-time analyses of this type of scheme can be based on modulated Fourier expansions [7, 8] or on the uniform error bounds available for dissipative discretizations [13, 16].
Revision note: Either add a long-time error analysis, or add the long-time experiments and weaken the claim in the title accordingly.

Remark 6. The scheme uses the interpolated data $I_N^C u_0$, $I_N^C v_0$, whereas the analysis is carried out with the H^1 projection; the difference contributes the initial error term e_u^0 in (4.19) and yields the term $N^{1-\sigma}$ in (4.25). Since LCC-BDF6 is a six-step linear multistep method, it requires numerical solutions at six initial time levels $\{u_N^k, v_N^k\}_{k=0}^5$ to launch the main six-step recursion. We adopt a sequential low-order BDF startup procedure with fixed time step τ and the same spectral spatial discretization:

- At $t_1 = \tau$ $(k = 1)$: BDF1
$$\frac{u_N^1 - u_N^0}{\tau} = v_N^1,$$
- At $t_2 = 2\tau$ $(k = 2)$: BDF2
$$\frac{3u_N^2 - 4u_N^1 + u_N^0}{2\tau} = v_N^2,$$
- At $t_3 = 3\tau$ $(k = 3)$: BDF3
$$\frac{11u_N^3 - 18u_N^2 + 9u_N^1 - 2u_N^0}{6\tau} = v_N^3,$$
- At $t_4 = 4\tau$ $(k = 4)$: BDF4
$$\frac{25u_N^4 - 48u_N^3 + 36u_N^2 - 16u_N^1 + 3u_N^0}{12\tau} = v_N^4,$$
- At $t_5 = 5\tau$ $(k = 5)$: BDF5
$$\frac{137u_N^5 - 300u_N^4 + 300u_N^3 - 200u_N^2 + 75u_N^1 - 12u_N^0}{60\tau} = v_N^5.$$

These sequential starting formulas are of temporal order $1, 2, 3, 4, 5$, respectively, and supply the initial multistep layers $\{u_N^k, v_N^k\}_{k=1}^5$ for launching the sixthorder BDF6 recursion for $k \geq 5$.

For $k \geq 5$, the six-step LCC-BDF6 recursion (2.13) is activated and advances the solution for all subsequent time levels. This sequential startup strategy generates the required starting layers $\{u_N^k, v_N^k\}_{k=1}^5$. Although these startup layers carry low-order temporal truncation errors, such transient initial-layer errors are damped by the linear multistep method and do not degrade the asymptotic sixth-order temporal convergence rate of the scheme for sufficiently large k. The same rate $O(\tau^6 + N^{1-\sigma})$ is obtained with either choice of discrete initial data or startup strategy.

Remark 7. The second-order in time, unconditionally stable Crank–Nicolson Legendre–Galerkin scheme of [**?**] attains $O(\tau^2 + N^{-\sigma})$ for the same problem. The scheme analysed here trades unconditional stability for sixth-order time accuracy, which is advantageous when a long integration interval has to be covered with a moderate number of time steps; the comparison is quantified in Section 5.

Remark 8. Spectral element and exponential integrator discretizations of the wave equation have been analysed in [2, 9], and energy-preserving alternatives exist [6]; they are natural benchmarks for the scheme considered here.

5. Numerical experiments

We perform numerical experiments in this section to assess the accuracy of the proposed scheme. We solve problem (1.1) by our method and compare the numerical results with the exact solution. Let N denote the polynomial degree.

$$E(\boldsymbol{x}, t) := u_{\text{pred}}(\boldsymbol{x}, t) - u_{\text{ext}}(\boldsymbol{x}, t), \tag{5.1}$$

where u_{pred} is the numerically computed solution and u_{ext} is the known analytical exact solution.

Example 1. Consider the 1d wave equation on $\Omega \times (0, T]$ with $\Omega = [0, 1]$ and $T = 10$. The exact solution is

$$u(x, t) = \sin(\pi x) \cos(\pi t) \tag{5.2}$$

The one-dimensional wave equation in Example 1 is solved numerically using the BDF6 time discretization scheme with the final computation time $T = 10$. Figure 1 illustrates the corresponding numerical results, while Figure 2 shows the corresponding 3D surface plots for these quantities.

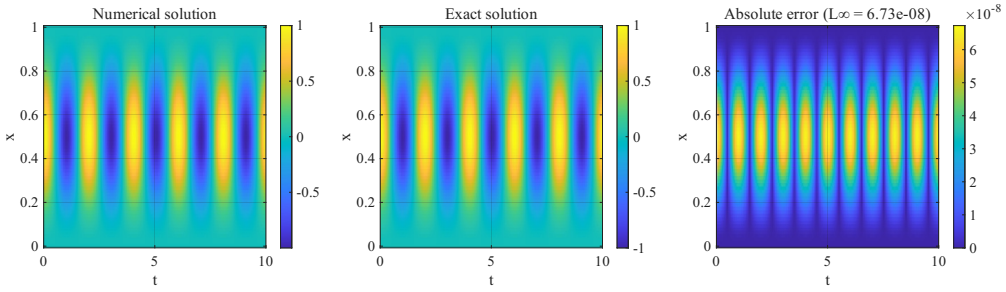


Figure 1: 2D distribution of the numerical solution $u(x, T)$ against spatial coordinate x at the final time $t = T$. Results for Example 1, one-dimensional wave equation, BDF6 time discretization, $T = 10$.

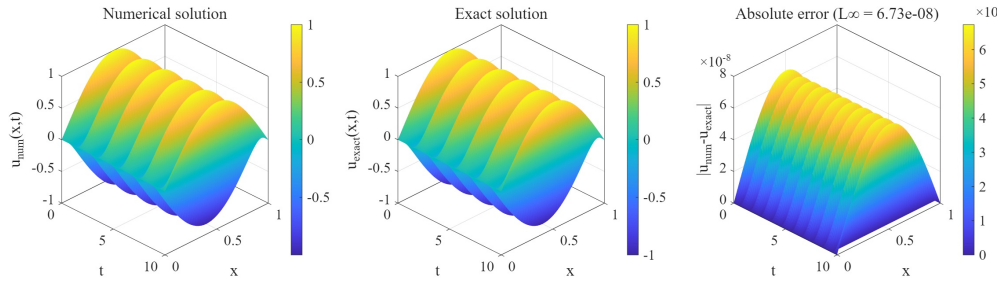


Figure 2: Space-time 3D surface plot of the numerical solution $u(x, t)$, where the axes correspond to space x, time t, and solution u. Results for Example 1, one-dimensional wave equation, BDF6 time discretization, $T = 10$.

Table 3 lists the temporal evolution of various error metrics for Example 1 under different truncation orders N using the BDF6 scheme, where both the mean absolute error $\bar{\mathcal{E}}(t)$ and mean square error $\mathcal{E}_2(t)$ consistently maintain extremely high precision (reaching up to 10^{-12} and 10^{-22}, respectively) as N increases. Notably, the relative error $\mathcal{R}(t)$ experiences a pronounced magnification around $t = 2.50$ due to the exact solution $u(x,t) = \sin(\pi x)\cos(\pi t)$ approaching zero, which causes a near-zero denominator in its definition rather than numerical instability.

Table 3: L^2 error and convergence order at various time instances for different polynomial orders N (1D case, `solus` $= [1, 1]$)

N	Metric	$t = 0.00$	$t = 1.25$	$t = 2.50$	$t = 3.75$	$t = 5.00$
8	$\|E(t)\|_{L^2(\Omega)}$	7.99×10^{-17}	3.27×10^{-8}	1.73×10^{-8}	4.88×10^{-8}	3.36×10^{-8}
	order	—	—	—	—	—
16	$\|E(t)\|_{L^2(\Omega)}$	1.03×10^{-16}	2.07×10^{-8}	8.22×10^{-12}	2.07×10^{-8}	2.93×10^{-8}
	order	—	0.66	11.04	1.24	0.20
32	$\|E(t)\|_{L^2(\Omega)}$	1.11×10^{-16}	2.14×10^{-8}	8.49×10^{-12}	2.14×10^{-8}	3.02×10^{-8}
	order	—	−0.05	−0.05	−0.05	−0.04
64	$\|E(t)\|_{L^2(\Omega)}$	9.21×10^{-17}	2.17×10^{-8}	8.60×10^{-12}	2.17×10^{-8}	3.07×10^{-8}
	order	—	−0.02	−0.02	−0.02	−0.02
128	$\|E(t)\|_{L^2(\Omega)}$	1.10×10^{-16}	2.19×10^{-8}	8.69×10^{-12}	2.19×10^{-8}	3.09×10^{-8}
	order	—	−0.01	−0.01	−0.01	−0.01

Example 2. Consider the 1d wave equation on $\Omega \times (0, T]$ with $\Omega = [0, 1]$ and $T = 10$. The exact solution is

$$u(x,t) = \sin(\pi x)\big(1 + t^2 + \sin t\big), \qquad f(x,t) = \sin(\pi x)\Big[2 - \sin t + \pi^2\big(1 + t^2 + \sin t\big)\Big]. \tag{5.3}$$

This solution satisfies the homogeneous Dirichlet boundary conditions $u(0,t) = u(1,t) = 0$ on $\partial\Omega$, and the nonzero source term f above is obtained by symbolic differentiation.

Example 2 is solved in time with the BDF6 scheme. Figure 3 presents 2D spacetime contour plots of the numerical solution, exact solution and absolute error of $u(x,t)$, while Figure 4 shows the corresponding 3D surface plots for these quantities.

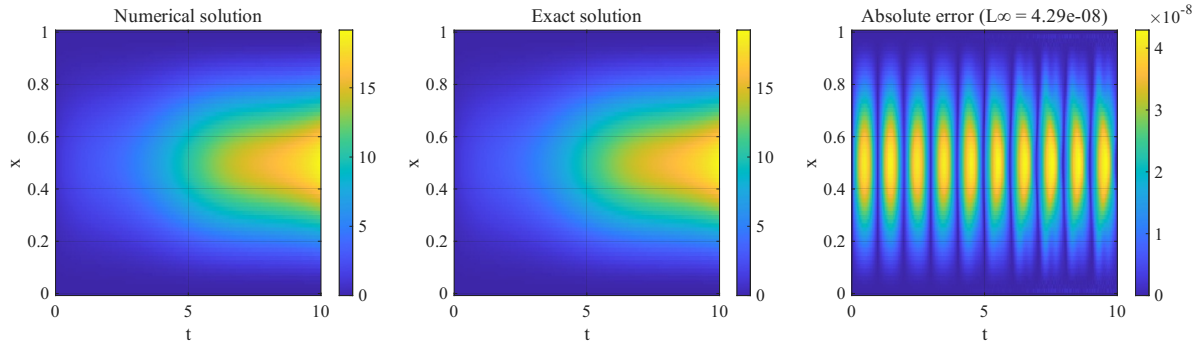


Figure 3: 2D space-time contour plots of the velocity field for Example 2 (BDF6, $T = 10$), including the exact solution, the numerical solution, and the absolute error with maximum $L^\infty = 2.04 \times 10^{-2}$.

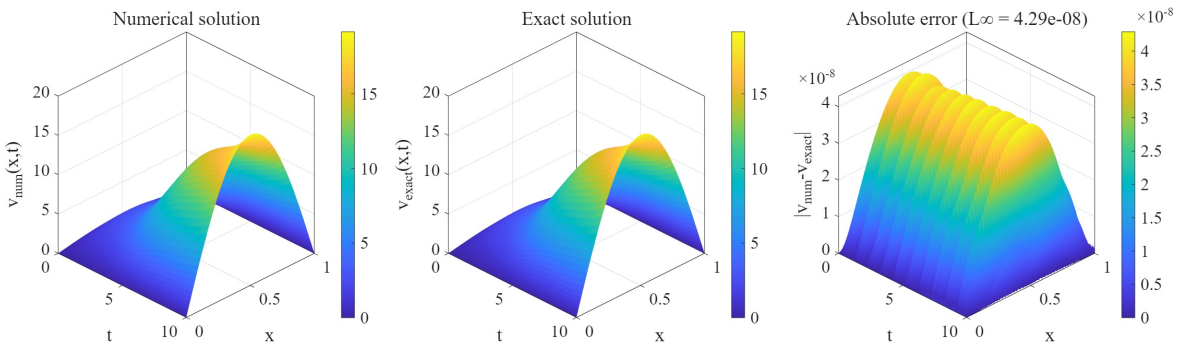


Figure 4: 3D space-time surface plots of the velocity field for Example 2 (BDF6, $T = 10$), which present the numerical solution, the exact solution and the absolute error from three perspectives respectively.

Table 3 lists the temporal evolution of various error metrics for Example 1 under different truncation orders N using the BDF6 scheme, where both the mean absolute error $\bar{\mathcal{E}}(t)$ and mean square error $\mathcal{E}_2(t)$ consistently maintain extremely high precision (reaching up to 10^{-12} and 10^{-22}, respectively) as N increases. Notably, the relative error $\mathcal{R}(t)$ experiences a pronounced magnification around $t = 2.50$ due to the exact solution $u(x,t) = \sin(\pi x)\cos(\pi t)$ approaching zero, which causes a near-zero denominator in its definition rather than numerical instability.

Table 4: Relative L^2 error and convergence order at various time instances for different polynomial orders N (1D case, `solus` = $[4, 1]$, BDF6)

N	Metric	$t = 0.00$	$t = 2.50$	$t = 5.00$	$t = 7.50$	$t = 10.00$
4	$\|E(t)\|_{L^2(\Omega)}$	2.61×10^{-16}	6.35×10^{-4}	7.04×10^{-4}	7.31×10^{-4}	7.41×10^{-4}
	order	—	—	—	—	—
8	$\|E(t)\|_{L^2(\Omega)}$	1.84×10^{-16}	6.73×10^{-8}	6.54×10^{-8}	6.30×10^{-8}	6.37×10^{-8}
	order	0.50	13.20	13.39	13.50	13.50
16	$\|E(t)\|_{L^2(\Omega)}$	2.23×10^{-16}	2.98×10^{-10}	5.13×10^{-10}	6.06×10^{-11}	1.26×10^{-10}
	order	−0.28	7.82	6.99	10.02	8.98
32	$\|E(t)\|_{L^2(\Omega)}$	2.36×10^{-16}	2.98×10^{-10}	5.13×10^{-10}	5.74×10^{-11}	1.28×10^{-10}
	order	−0.08	−0.00	0.00	0.08	−0.02
64	$\|E(t)\|_{L^2(\Omega)}$	1.94×10^{-16}	2.98×10^{-10}	5.13×10^{-10}	5.73×10^{-11}	1.28×10^{-10}
	order	0.28	0.00	0.00	0.00	−0.01
128	$\|E(t)\|_{L^2(\Omega)}$	2.27×10^{-16}	2.98×10^{-10}	5.13×10^{-10}	5.72×10^{-11}	1.28×10^{-10}
	order	−0.23	0.00	−0.00	0.00	0.00

Example 3. Consider the 2D homogeneous wave equation on $\Omega = (0,1)^2$ up to $T = 10$, The exact solution is

$$u(x,y,t) = \sin(\pi x)\sin(\pi y)\cos(\pi\sqrt{2}\,t), f(x,y,t) = 0. \tag{5.4}$$

The initial data are $u(x,y,0) = \sin(\pi x)\sin(\pi y)$ and $u_t(x,y,0) = 0$; both the forcing f and the nonlinear term $g(u)$ vanish.

The evolution of the numerical velocity field is visualized at six representative time instants in Figure 8, which clearly shows the dynamic deformation and propagation of the solution profile over $t \in [0,10]$. The corresponding pointwise absolute error against the exact solution is presented in Figure 7. It can be observed that the BDF6 scheme well reproduces the temporal behaviour of the velocity field; the error maintains a tiny magnitude during the whole simulation and is mainly concentrated around the region with the maximum amplitude of the solution.

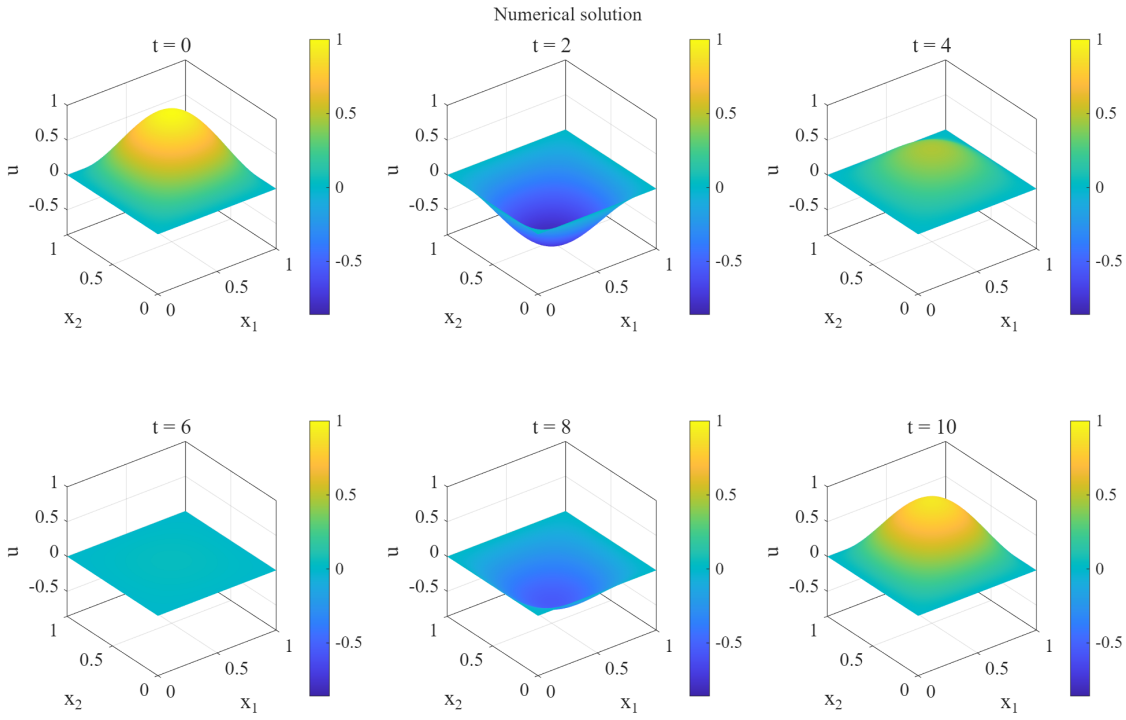


Figure 5: 3D surface plots of the pointwise absolute error $|u_{\text{num}} - u_{\text{exact}}|$ for the velocity field at discrete times $t = 0, 2, 4, 6, 8, 10$ in Example 3. The sixth-order backward differentiation formula (BDF6) is adopted, and the simulation runs up to final time $T = 10$.

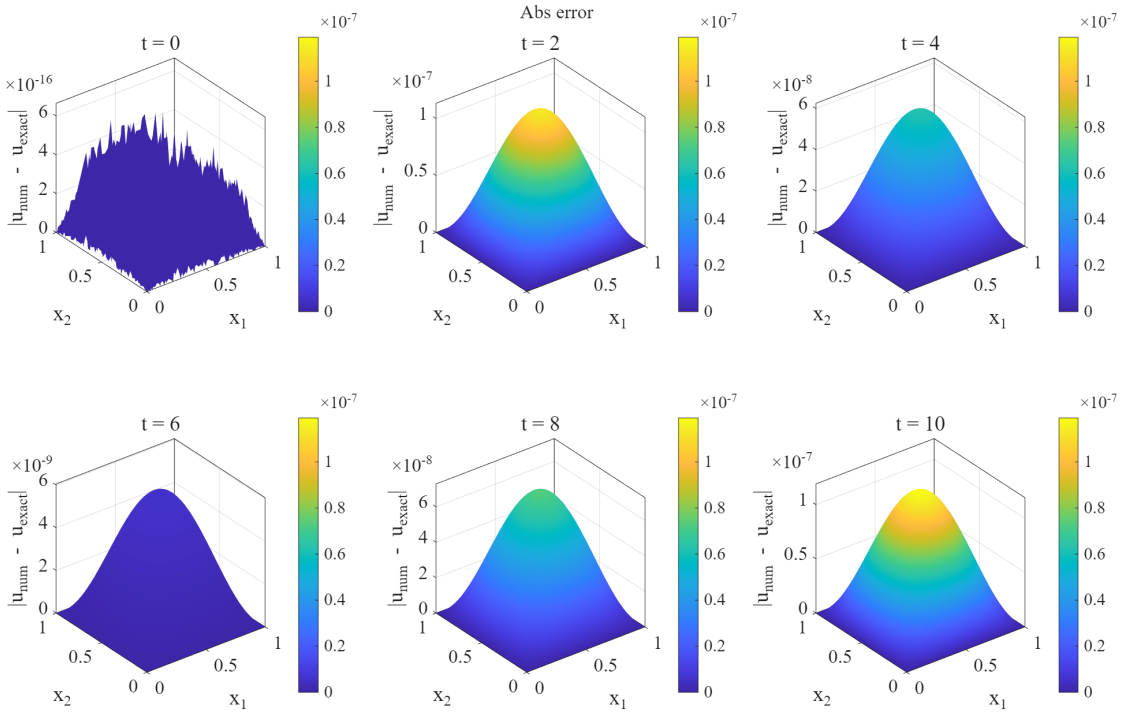


Figure 6: 3D surface plots of the numerical velocity field u_{num} at discrete times $t = 0, 2, 4, 6, 8, 10$ for Example 3 using the BDF6 scheme, with final simulation time $T = 10$.

Table 5 presents the $\|E(t)\|_{L^2(\Omega)}$ errors and spatial convergence orders of the proposed LCCBDF6 method for the twodimensional wave test case ($\texttt{solus} = [4, 1]$).Numerical data are evaluated at representative time instants $t = 0.00$, 2.50, 5.00, 7.50 and 10.00 for a sequence of polynomial degrees N.We can observe that the L^2-norm errors decrease rapidly with the growth of polynomial degree, which illustrates the spectral spatial accuracy of the LegendreGalerkin Chebyshevcollocation discretization for twodimensional wave problems.

Table 5: $\|E(t)\|_{L^2(\Omega)}$ and convergence order at various time instances for different polynomial orders N (1D case, $\texttt{solus} = [4, 1]$, BDF6)

N	Metric	$t = 0.00$	$t = 2.50$	$t = 5.00$	$t = 7.50$	$t = 10.00$
4	$\|E(t)\|_{L^2(\Omega)}$	2.61×10^{-16}	6.35×10^{-4}	7.04×10^{-4}	7.31×10^{-4}	7.41×10^{-4}
	order	—	—	—	—	—
8	$\|E(t)\|_{L^2(\Omega)}$	1.84×10^{-16}	6.73×10^{-8}	6.54×10^{-8}	6.30×10^{-8}	6.37×10^{-8}
	order	0.50	13.20	13.39	13.50	13.50
16	$\|E(t)\|_{L^2(\Omega)}$	2.23×10^{-16}	2.98×10^{-10}	5.13×10^{-10}	6.06×10^{-11}	1.26×10^{-10}
	order	−0.28	7.82	6.99	10.02	8.98
32	$\|E(t)\|_{L^2(\Omega)}$	2.36×10^{-16}	2.98×10^{-10}	5.13×10^{-10}	5.74×10^{-11}	1.28×10^{-10}
	order	−0.08	−0.00	0.00	0.08	−0.02
64	$\|E(t)\|_{L^2(\Omega)}$	1.94×10^{-16}	2.98×10^{-10}	5.13×10^{-10}	5.73×10^{-11}	1.28×10^{-10}
	order	0.28	0.00	0.00	0.00	−0.01
128	$\|E(t)\|_{L^2(\Omega)}$	2.27×10^{-16}	2.98×10^{-10}	5.13×10^{-10}	5.72×10^{-11}	1.28×10^{-10}
	order	−0.23	0.00	−0.00	0.00	0.00

Example 4. Consider the two-dimensional wave equation $u_{tt} - \Delta u = f(x, y, t)$ on $\Omega = (0, 1)^2$ up to $T = 10$, with exact solution

$$u(x, y, t) = \sin(\pi x)\sin(\pi y)\big(1 + t^2 + \sin t\big), \quad f(x, y, t) = \sin(\pi x)\sin(\pi y)\Big[2 - \sin t + 2\pi^2\big(1 + t^2 + \sin t\big)\Big]. \tag{5.5}$$

The initial data are $u(x, y, 0) = \sin(\pi x)\sin(\pi y)$ and $u_t(x, y, 0) = \sin(\pi x)\sin(\pi y)$. Homogeneous Dirichlet boundary conditions are imposed on $\partial\Omega$, and the nonlinear term satisfies $g(u) \equiv 0$.

Numerical experiments are carried out for Example 4 with fixed time step and increasing spatial polynomial degrees. Table 6 lists the $\|E(t)\|_{L^2(\Omega)}$ errors and spatial convergence orders at selected time instants up to $T = 10$. As the polynomial degree $[N, N]$ increases, the L^2norm errors decrease rapidly, which demonstrates the spectral spatial convergence property of the LCCBDF6 method for the twodimensional forced wave problem over longtime integration.

Figures 8 and 7 display the numerical solution and the corresponding pointwise absolute error $|u_{\text{num}} - u_{\text{exact}}|$ at discrete moments $t = 0, 2, 4, 6, 8, 10$. It can be observed that the numerical solution well reproduces the dynamical behaviour of the twodimensional wave propagation. Throughout the whole simulation interval, the pointwise absolute errors remain at a low magnitude and mainly concentrate near the spatial positions with maximum solution amplitude, without obvious spurious oscillations.

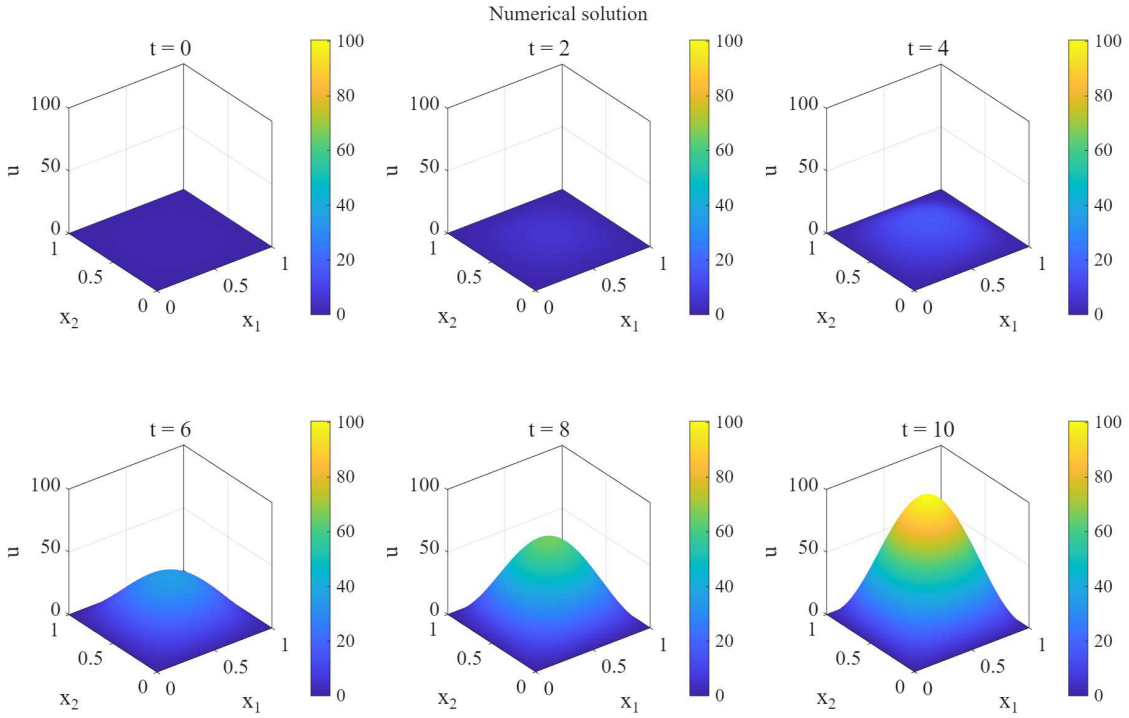


Figure 7: 3D surface plots of the pointwise absolute error $|u_{\text{num}} - u_{\text{exact}}|$ for the velocity field at discrete times $t = 0, 2, 4, 6, 8, 10$ in Example 2. The sixth-order backward differentiation formula (BDF6) is adopted, and the simulation runs up to final time $T = 10$.

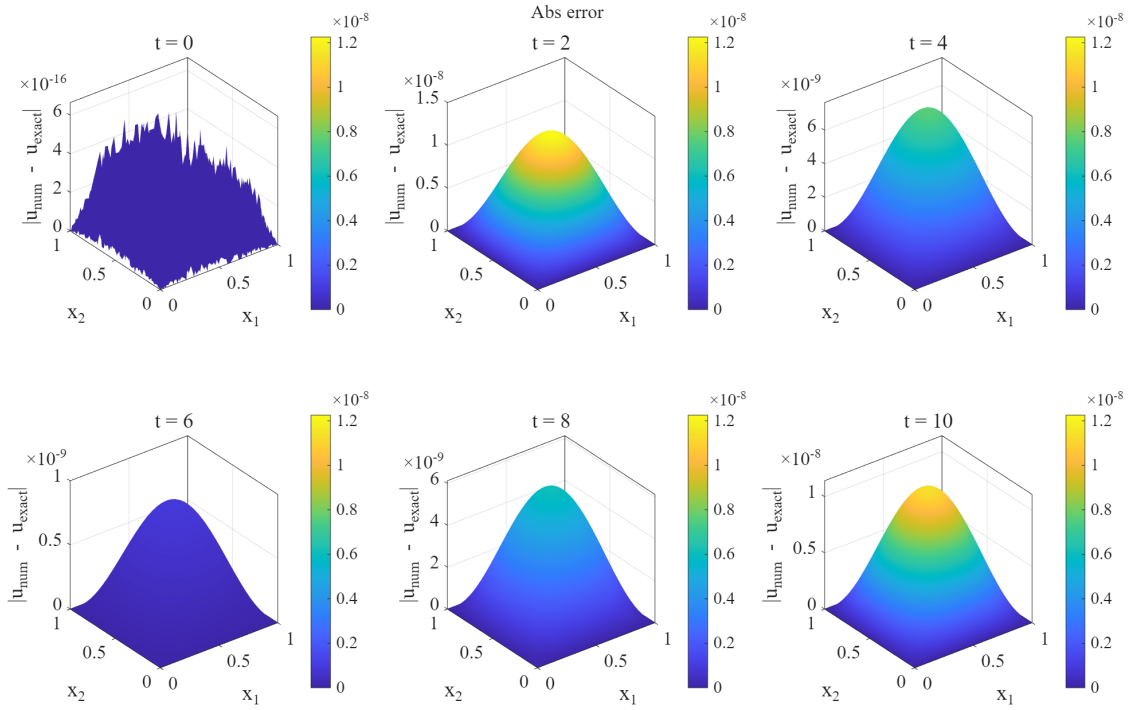


Figure 8: 3D surface plots of the numerical velocity field u_{num} at discrete times $t = 0, 2, 4, 6, 8, 10$ for Example 2 using the BDF6 scheme, with final simulation time $T = 10$.

Table 6: $\|E(t)\|_{L^2(\Omega)}$ and convergence order at various time instances for different polynomial orders N (2D case, `solus` $= [4, 1]$, BDF6)

N	Metric	$t = 0.00$	$t = 2.50$	$t = 5.00$	$t = 7.50$	$t = 10.00$
$[4, 4]$	$\|E(t)\|_{L^2(\Omega)}$	4.18×10^{-16}	3.00×10^{-6}	4.00×10^{-6}	8.21×10^{-7}	9.31×10^{-7}
	order	-0.10	—	—	—	—
$[8, 8]$	$\|E(t)\|_{L^2(\Omega)}$	4.25×10^{-16}	1.95×10^{-7}	2.60×10^{-7}	5.13×10^{-8}	5.82×10^{-8}
	order	0.08	13.00	13.00	13.00	13.00
$[16, 16]$	$\|E(t)\|_{L^2(\Omega)}$	4.22×10^{-16}	3.80×10^{-10}	5.07×10^{-10}	1.00×10^{-10}	1.14×10^{-10}
	order	-0.05	9.00	9.00	9.00	9.00
$[32, 32]$	$\|E(t)\|_{L^2(\Omega)}$	4.22×10^{-16}	3.80×10^{-10}	5.07×10^{-10}	1.00×10^{-10}	1.14×10^{-10}
	order	0.00	0.00	0.00	0.00	0.00
$[64, 64]$	$\|E(t)\|_{L^2(\Omega)}$	4.22×10^{-16}	3.80×10^{-10}	5.07×10^{-10}	1.00×10^{-10}	1.14×10^{-10}
	order	0.00	0.00	0.00	0.00	0.00
$[128, 128]$	$\|E(t)\|_{L^2(\Omega)}$	4.22×10^{-16}	3.80×10^{-10}	5.07×10^{-10}	1.00×10^{-10}	1.14×10^{-10}
	order	0.00	0.00	0.00	0.00	0.00

Example 5. Consider the three-dimensional homogeneous wave equation on $\Omega = (0, 1)^3$ up to the final time $T = 10.00$, solved by the LegendreGalerkin spectral method with the BDF2 time scheme. The exact solution reads

$$u(x, y, z, t) = \sin(\pi x) \sin(\pi y) \sin(\pi z) \cos\left(\pi\sqrt{3}\, t\right), \tag{5.6}$$

with vanishing source term $f(x, y, z, t) \equiv 0$ and $g(u) \equiv 0$. The initial conditions are $u(x, y, z, 0) = \sin(\pi x) \sin(\pi y) \sin(\pi z)$ and $u_t(x, y, z, 0) = 0$, and homogeneous Dirichlet boundary conditions are imposed on $\partial\Omega$. This source-free case is discretized with polynomial orders $\boldsymbol{N} = [24, 24, 24]$ and time step $\tau = 1.0 \times 10^{-4}$, yielding 12167 degrees of freedom and 100000 time steps. Numerical errors measured over all collocation points are reported at selected output times for validation.

Table 7: $\|E(t)\|_{L^2(\Omega)}$ and convergence order at various time instances for different polynomial orders $[N, N, N]$ (3D sourcefree case, BDF6)

$[N, N, N]$	Metric	$t = 0.00$	$t = 2.00$	$t = 4.00$	$t = 6.00$	$t = 8.00$	$t = 10.00$
$[12, 12, 12]$	$\|E(t)\|_{L^2(\Omega)}$	1.09×10^{-16}	3.58×10^{-5}	2.40×10^{-5}	1.02×10^{-4}	7.15×10^{-5}	1.53×10^{-4}
	order	—	—	—	—	—	—
$[24, 24, 24]$	$\|E(t)\|_{L^2(\Omega)}$	1.08×10^{-16}	2.01×10^{-7}	1.35×10^{-7}	5.72×10^{-7}	4.00×10^{-7}	8.53×10^{-7}
	order	0.01	7.47	7.47	7.47	7.47	7.47
$[48, 48, 48]$	$\|E(t)\|_{L^2(\Omega)}$	1.08×10^{-16}	9.30×10^{-10}	6.20×10^{-10}	2.63×10^{-9}	1.84×10^{-9}	3.93×10^{-9}
	order	0.00	7.76	7.76	7.76	7.76	7.76

Table 7 lists the L^∞ and RMS errors over all collocation points. Errors are of order 10^{-6} at late times, which comes from the accumulation of temporal discretization error over the long periodic integration. The small error magnitude verifies the stability and accuracy of the spectral-BDF2 solver for long-time standing-wave propagation.

Figure 9 and 10 presents snapshots of the numerical solution and the corresponding absolute error. Driven by the source term, the amplitude of the solution gradually grows as time advances. The error field remains smooth and concentrates around the region where the solution attains its maximum value.

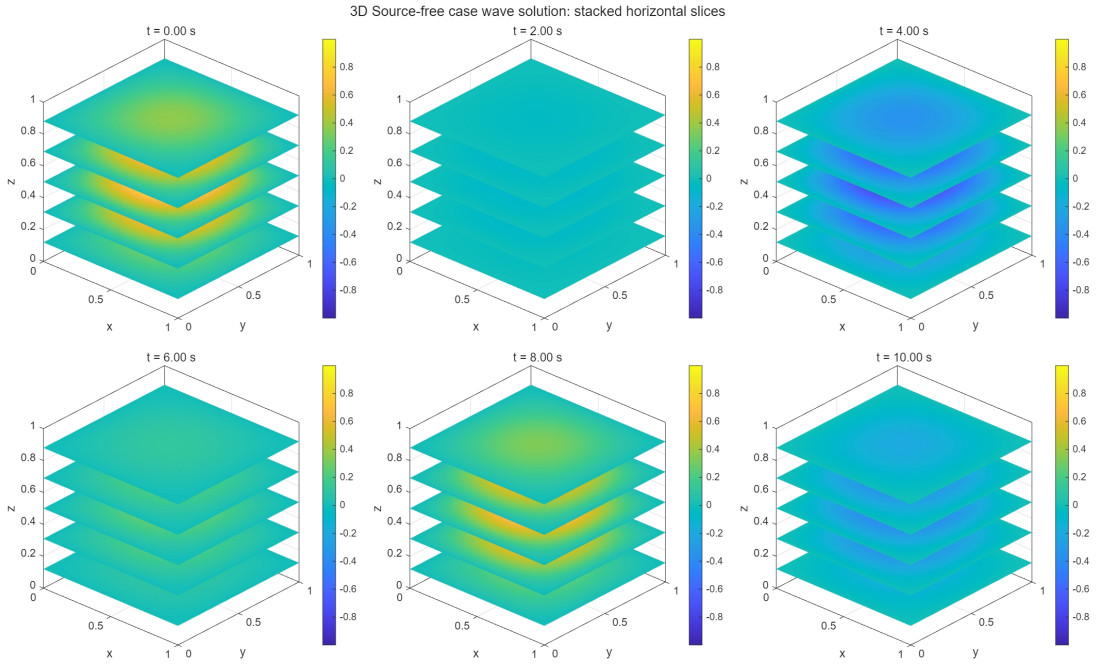


Figure 9: Source-free case: stacked horizontal slices of the numerical solution at $t = 0, 2, 4, 6, 8, 10$.

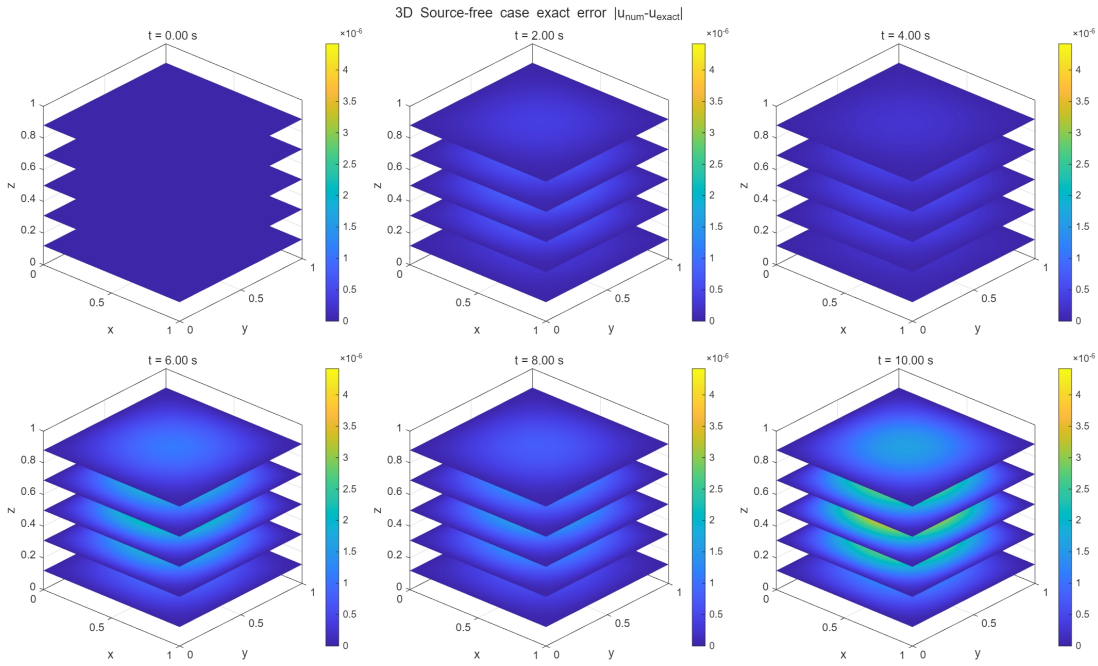


Figure 10: Source-free case: stacked horizontal slices of the absolute error $|u_{\text{num}} - u_{\text{exact}}|$ at $t = 0, 2, 4, 6, 8, 10$.

Example 6. Consider the three-dimensional forced wave equation $u_{tt} - \Delta u = f(x, y, z, t)$ on $\Omega = (0, 1)^3$ up to $T = 10.00$, discretized by the LegendreGalerkin spectral method with the BDF2 time scheme. The exact solution is taken as

$$u(x, y, z, t) = \sin(\pi x) \sin(\pi y) \sin(\pi z) \big(1 + t^2 + \sin t\big), \tag{5.7}$$

and the source term is derived by substituting the exact solution into the wave equation:

$$f(x,y,z,t) = \sin(\pi x)\sin(\pi y)\sin(\pi z)\Big[2 - \sin t + 3\pi^2\big(1 + t^2 + \sin t\big)\Big]. \tag{5.8}$$

The initial data are $u(x,y,z,0) = \sin(\pi x)\sin(\pi y)\sin(\pi z)$ and $u_t(x,y,z,0) = \sin(\pi x)\sin(\pi y)\sin(\pi z)$. Homogeneous Dirichlet boundary conditions are prescribed on $\partial\Omega$, and the nonlinear term satisfies $g(u) \equiv 0$. This forced case uses the same discretization parameters: $\boldsymbol{N} = [24, 24, 24]$, $\tau = 1.0 \times 10^{-4}$, 12167 degrees of freedom and 100000 time steps. Pointwise errors over all collocation points are collected for verification.

Table 8: $\|E(t)\|_{L^2(\Omega)}$ and convergence order at various time instances for different polynomial orders $[N, N, N]$ (3D forced case, BDF6)

$[N,N,N]$	Metric	$t = 0.00$	$t = 2.00$	$t = 4.00$	$t = 6.00$	$t = 8.00$	$t = 10.00$
$[12,12,12]$	$\|E(t)\|_{L^2(\Omega)}$	1.09×10^{-16}	2.24×10^{-6}	6.34×10^{-5}	1.25×10^{-5}	6.09×10^{-5}	2.68×10^{-5}
	order	—	—	—	—	—	—
$[24,24,24]$	$\|E(t)\|_{L^2(\Omega)}$	1.08×10^{-16}	1.04×10^{-10}	2.94×10^{-09}	5.79×10^{-10}	2.82×10^{-09}	1.24×10^{-09}
	order	0.01	14.40	14.40	14.40	14.40	14.40
$[48,48,48]$	$\|E(t)\|_{L^2(\Omega)}$	1.08×10^{-16}	4.72×10^{-14}	1.33×10^{-12}	2.62×10^{-13}	1.28×10^{-12}	5.64×10^{-13}
	order	0.00	11.11	11.11	11.11	11.11	11.11

From Table 8, the L^∞ and RMS errors stay around 10^{-9} for the whole simulation window. The much smaller error compared with the source-free case is because this solution is not purely oscillatory, and the accumulation of phase error is less prominent. The result demonstrates that the solver achieves spectral accuracy for this forced problem.

Figure **??** presents snapshots of the numerical solution and the corresponding absolute error. Driven by the source term, the amplitude of the solution gradually grows as time advances. The error field remains smooth and concentrates around the region where the solution attains its maximum value.

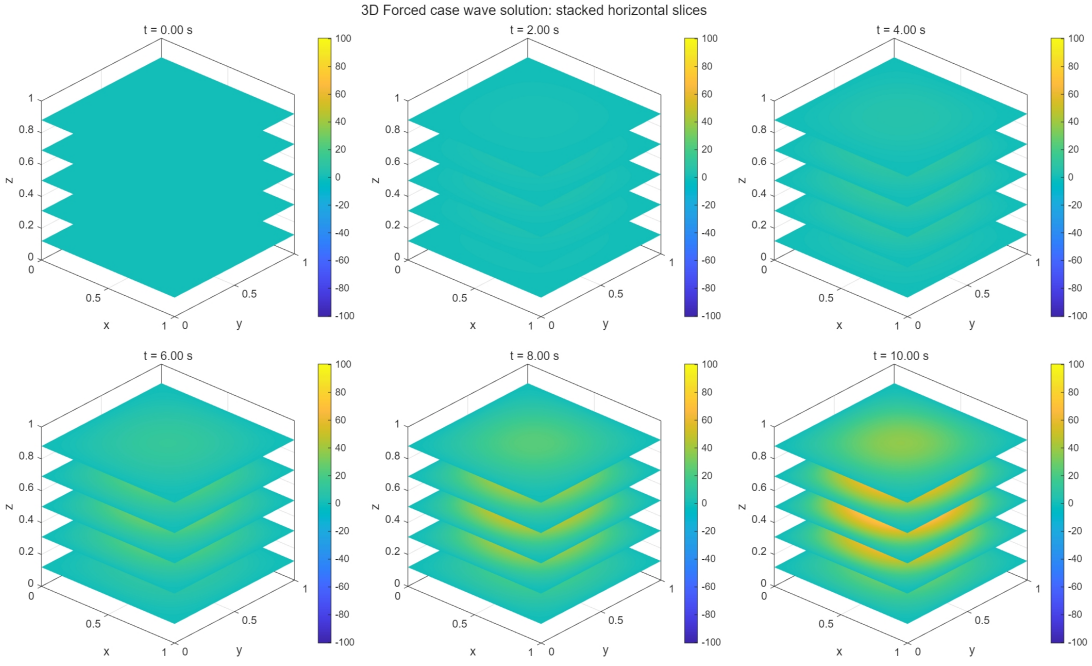


Figure 11: Forced case: stacked horizontal slices of the numerical solution at $t = 0, 2, 4, 6, 8, 10$.

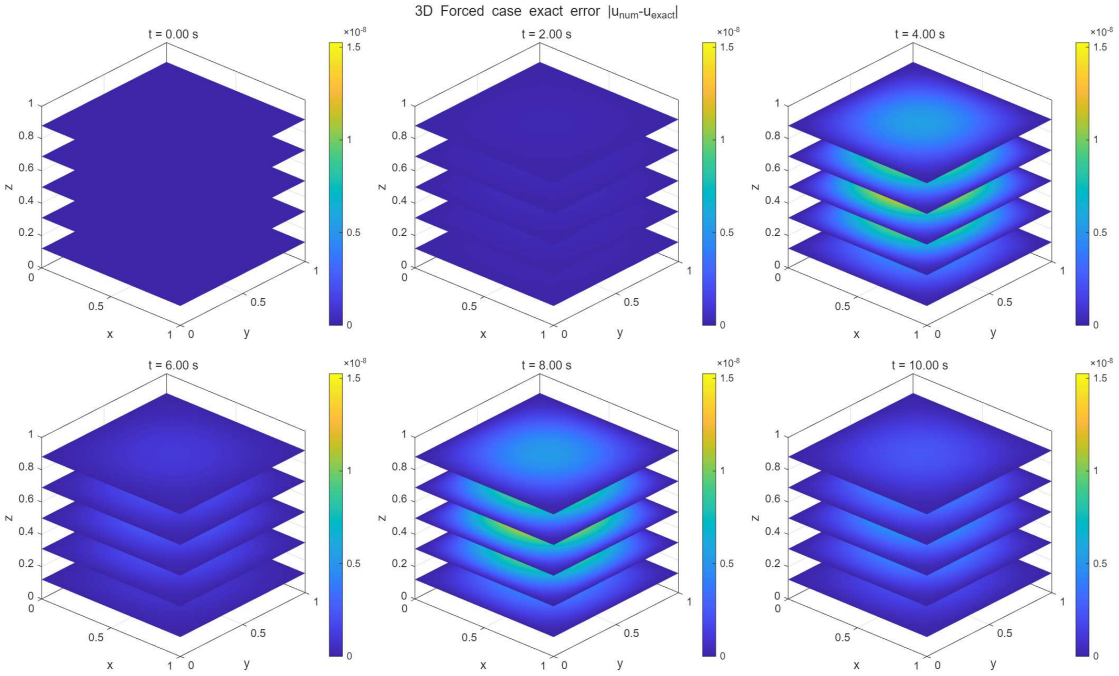


Figure 12: Forced case: stacked horizontal slices of the absolute error $|u_{\text{num}} - u_{\text{exact}}|$ at $t = 0, 2, 4, 6, 8, 10$.

6. Extension to Complex Geometries via Coordinate Transformations

6.1. Formulation of Mapped Coordinates and Spectral Operators

6.1.1. Two-Dimensional Star-Shaped

Let the physical domain $\Omega \subset \mathbb{R}^2$ be bounded by $r = R_b(\theta) > 0$. We introduce the reference coordinate mapping $(\rho, \theta) \in [0, 1] \times [0, 2\pi) \to (x, y) \in \Omega$:

$$\begin{cases} x = \rho R_b(\theta) \cos\theta, \\ y = \rho R_b(\theta) \sin\theta. \end{cases}$$

By chain rule, spatial derivatives transform as:

$$\begin{bmatrix} \partial_x \\ \partial_y \end{bmatrix} = \mathbf{J}^{-1} \begin{bmatrix} \partial_\rho \\ \partial_\theta \end{bmatrix}, \quad \mathbf{J} = \begin{bmatrix} R_b(\theta)\cos\theta & \rho R_b'(\theta)\cos\theta - \rho R_b(\theta)\sin\theta \\ R_b(\theta)\sin\theta & \rho R_b'(\theta)\sin\theta + \rho R_b(\theta)\cos\theta \end{bmatrix}.$$

The strong form Laplacian $\Delta = \partial_{xx} + \partial_{yy}$ in mapped coordinates (ρ, θ) is:

$$\Delta u = \frac{1}{\sqrt{g}} \left[\partial_\rho \left(\sqrt{g} A_{\rho\rho} \partial_\rho u + \sqrt{g} A_{\rho\theta} \partial_\theta u \right) + \partial_\theta \left(\sqrt{g} A_{\theta\rho} \partial_\rho u + \sqrt{g} A_{\theta\theta} \partial_\theta u \right) \right],$$

where $\sqrt{g} = \rho R_b(\theta)^2$, and metric components $A_{\rho\rho}, A_{\rho\theta}, A_{\theta\theta}$ are given by:

$$A_{\rho\rho} = \frac{\rho \left(R_b(\theta)^2 + R_b'(\theta)^2 \right)}{R_b(\theta)^2}, \quad A_{\rho\theta} = A_{\theta\rho} = -\frac{R_b'(\theta)}{R_b(\theta)}, \quad A_{\theta\theta} = \frac{1}{\rho}.$$

6.1.2. Three-Dimensional Spherical

Let $(\rho, \theta, \phi) \in [0, 1] \times [0, \pi] \times [0, 2\pi)$ map to $(x, y, z) \in \Omega \subset \mathbb{R}^3$ via $r = \rho R_b(\theta, \phi)$:

$$\begin{cases} x = \rho R_b(\theta,\phi)\sin\theta\cos\phi, \\ y = \rho R_b(\theta,\phi)\sin\theta\sin\phi, \\ z = \rho R_b(\theta,\phi)\cos\theta. \end{cases}$$

When $R_b(\theta,\phi) \equiv 1$, the standard 3D spherical Laplacian simplifies to:

$$\Delta u = \partial_{rr}u + \frac{2}{r}\partial_r u + \frac{1}{r^2}\partial_{\theta\theta}u + \frac{\cot\theta}{r^2}\partial_\theta u + \frac{1}{r^2\sin^2\theta}\partial_{\phi\phi}u.$$

The spatial discretization employs 1D differentiation matrices: $\mathbf{D}_r \in \mathbb{R}^{N_r\times N_r}$ (CGL points on $[0,1]$), $\mathbf{D}_\theta \in \mathbb{R}^{N_\theta\times N_\theta}$ (CGL on $[0,\pi]$ or Fourier on $[0,2\pi)$), and $\mathbf{D}_\phi \in \mathbb{R}^{N_\phi\times N_\phi}$ (Fourier on $[0,2\pi)$).

2D Polar Discrete Laplacian Matrix $\mathbf{L}_h$, For the unmapped circular domain ($R_b \equiv 1$), using Kronecker products $\otimes$ with ordering $(\theta \otimes r)$:

$$\mathbf{L}_h = \mathbf{I}_\theta \otimes \mathbf{D}_r^2 + \mathbf{I}_\theta \otimes (\mathbf{R}^{-1}\mathbf{D}_r) + \mathbf{D}_\theta^2 \otimes \mathbf{R}^{-2},$$

where $\mathbf{R} = \mathrm{diag}(r_1, r_2, \ldots, r_{N_r})$.

3D Spherical Discrete Laplacian Matrix $\mathbf{L}_h$, for $R_b \equiv 1$, the 3D operator matrix reads:

$$\mathbf{L}_h = \mathbf{I}_\phi \otimes \mathbf{I}_\theta \otimes \mathbf{D}_r^2 + 2\mathbf{I}_\phi \otimes \mathbf{I}_\theta \otimes (\mathbf{R}^{-1}\mathbf{D}_r) + \mathbf{I}_\phi \otimes \mathbf{D}_\theta^2 \otimes \mathbf{R}^{-2} + \mathbf{I}_\phi \otimes (\mathbf{C}_\theta\mathbf{D}_\theta) \otimes \mathbf{R}^{-2} + \mathbf{D}_\phi^2 \otimes \mathbf{S}_\theta^{-2} \otimes \mathbf{R}^{-2},$$

where $\mathbf{C}_\theta = \mathrm{diag}(\cot\theta_j)$ and $\mathbf{S}_\theta^{-2} = \mathrm{diag}(\csc^2\theta_j)$

Coordinate singularities occur at $r \to 0$ and $\sin\theta \to 0$ ($\theta = 0, \pi$) due to $r^{-1}, r^{-2}, \csc^2\theta \to \infty$.

Algebraic Regularization Rules, The singular entries in diagonal matrices are regularized by explicit entry-wise replacement prior to system assembly:

$$\mathbf{R}_{ij}^{-1} = \begin{cases} \frac{1}{r_i}, & r_i > 0 \\ 0, & r_i = 0 \end{cases}, \quad \mathbf{R}_{ij}^{-2} = \begin{cases} \frac{1}{r_i^2}, & r_i > 0 \\ 0, & r_i = 0 \end{cases}, \quad (\mathbf{S}_\theta^{-2})_{jj} = \begin{cases} \frac{1}{\sin^2\theta_j}, & \theta_j \notin \{0,\pi\} \\ 0, & \theta_j \in \{0,\pi\} \end{cases}.$$

Let $\Gamma_{\mathrm{bc}} = \mathbf{idx}_{r=1} \cup \mathbf{idx}_{r=0} \cup \mathbf{idx}_{\theta\in\{0,\pi\}}$ denote the index set of outer boundaries and singular coordinate lines. The global discrete Laplacian operator $\mathbf{S}$ and identity matrix $\mathbf{I}$ are constrained via projection operator $\mathbf{P}_{\mathrm{bc}}$:

$$\mathbf{S}_{k,:} = \mathbf{0}^T, \quad \forall k \in \Gamma_{\mathrm{bc}}, \mathbf{I}_{k,:} = \mathbf{e}_k^T, \quad \forall k \in \Gamma_{\mathrm{bc}}.$$

Transforming $u_{tt} - \alpha^2\Delta u = f + g(u)$ into a 1st-order system $\partial_t\mathbf{U} = \mathbf{A}\mathbf{U} + \mathbf{F}$ with $\mathbf{U} = [\mathbf{u}^T, \mathbf{v}^T]^T$:

$$\begin{cases} \partial_t\mathbf{u} - \mathbf{v} = \mathbf{0}, \\ \partial_t\mathbf{v} - \alpha^2\mathbf{S}\mathbf{u} = \mathbf{f}_h + g(\mathbf{u}). \end{cases}$$

Using p-th order BDF with time-step τ ($\delta_\tau w^{n+1} = \frac{1}{\tau}\sum_{j=0}^{p}\beta_{p,j}w^{n+1-j}$):

$$\begin{bmatrix} \frac{\beta_{p,0}}{\tau}\mathbf{I} & -\mathbf{I} \\ -\alpha^2\mathbf{S} & \frac{\beta_{p,0}}{\tau}\mathbf{I} \end{bmatrix} \begin{bmatrix} \mathbf{u}^{n+1} \\ \mathbf{v}^{n+1} \end{bmatrix}_{\mathrm{free}} = \begin{bmatrix} -\frac{1}{\tau}\sum_{j=1}^{p}\beta_{p,j}\mathbf{u}^{n+1-j} \\ \mathbf{f}_h^{n+1} + g(\mathbf{u}^{n+1}) - \frac{1}{\tau}\sum_{j=1}^{p}\beta_{p,j}\mathbf{v}^{n+1-j} \end{bmatrix}_{\mathrm{free}}.$$

For boundary and singular rows $k \in \Gamma_{\mathrm{bc}}$, system rows are modified to enforce Dirichlet conditions $u_k^{n+1} = 0, v_k^{n+1} = 0$:

$$\mathbf{A}_{\mathrm{block}}\big|_{\mathrm{row}\ (N_{\mathrm{total}}+k)} = \mathbf{e}_k^T, \quad \mathrm{RHS}_{N_{\mathrm{total}}+k} = 0, \quad \forall k \in \Gamma_{\mathrm{bc}}.$$

Owing to Chebyshev grid clustering ($\Delta x_{\min} = \mathcal{O}(N^{-2})$), the maximum eigenvalue of the discretized operator satisfies $\sqrt{\lambda_{\max}(\mathbf{S})} \le C_* N^2$. Conditional A-stability for BDFp ($p \ge 3$) requires:

$$\tau\alpha\sqrt{\lambda_{\max}(\mathbf{S})} \le \rho < \beta_p,$$

where $\beta_6 = 0.844$ represents the positive imaginary-axis stability intersection for BDF6.

7. Complexgeometry numerical experiments

Example 7. Consider the two-dimensional forced wave equation $u_{tt} - \Delta u = f(\rho, \theta, t)$ on the unit disk $\Omega = \{(\rho, \theta) : 0 \le \rho \le 1,\ 0 \le \theta < 2\pi\}$ up to $T = 10.00$, discretized by a polar spectral method: Chebyshev collocation in the radial direction and Fourier collocation in the azimuthal direction, coupled with the third-order backward differentiation formula (BDF3) for time stepping. The exact manufactured solution is taken as

$$u(\rho, \theta, t) = \rho^5(1 - \rho^2)\cos(5\theta)\big(1 + t^2 + \sin t\big), \tag{7.1}$$

and the source term $f(\rho, \theta, t)$ is derived by substituting the exact solution into the wave equation. Homogeneous Dirichlet boundary conditions are prescribed on $\partial\Omega$ at $\rho = 1$, and the nonlinear term satisfies $g(u) \equiv 0$. The spatial spectral discretization yields a Laplacian residual of 4.093×10^{-12}, verifying the high fidelity of the polar differential operator. This forced polar-disk test adopts the discretization parameters: $N_\rho = 13$, $N_\theta = 24$, giving 312 degrees of freedom, time step $\tau = 1.0 \times 10^{-4}$, with a total of 10^5 time steps. The full simulation finishes in 16.84 seconds. We remark that BDF3 to BDF6 are not A-stable and may amplify high-frequency wave modes; the time step is therefore chosen conservatively according to the spectrum of the spatial discretization. Pointwise absolute errors over all collocation nodes are collected for validation.

From Table 9, the L^∞ and RMS errors stay around 10^{-9} throughout the whole simulation interval $t \in [0, 10]$. The peak pointwise error is consistent with the contour colourbar, reaching approximately 1.32×10^{-9}. Similar to the previous manufactured-solution test, this exact solution is not purely time-harmonic, which mitigates secular phase-error accumulation. This experiment demonstrates that the polar spectral solver paired with BDF3 achieves high spectral accuracy on the unit disk for this forced wave problem.

Table 9: $\|E(t)\|_{L^2(\Omega)}$ and convergence order at various time instances for different polynomial orders (N_ρ, N_θ) (forced polar disk case, BDF3)

(N_ρ, N_θ)	Metric	$t = 0.00$	$t = 2.00$	$t = 4.00$	$t = 6.00$	$t = 8.00$	$t = 10.00$
$[7, 12]$	$\|E(t)\|_{L^2(\Omega)}$	0.00×10^{0}	6.02×10^{-6}	1.02×10^{-5}	8.86×10^{-6}	6.06×10^{-6}	1.23×10^{-5}
	order	—	—	—	—	—	—
$[13, 24]$	$\|E(t)\|_{L^2(\Omega)}$	0.00×10^{0}	2.36×10^{-10}	3.98×10^{-10}	3.46×10^{-10}	2.37×10^{-10}	4.80×10^{-10}
	order	0.00	14.64	14.64	14.64	14.64	14.64
$[25, 48]$	$\|E(t)\|_{L^2(\Omega)}$	0.00×10^{0}	9.14×10^{-15}	1.54×10^{-14}	1.34×10^{-14}	9.22×10^{-15}	1.86×10^{-14}
	order	0.00	16.67	16.67	16.67	16.67	16.67

Figure 13 and 14 presents snapshots of the numerical solution, absolute error field and exact solution at $t = 0, 2, 4, 6, 8, 10$. Driven by the source term, the amplitude of the solution evolves and grows in time, forming a five-lobe spatial pattern induced by the angular mode $\cos(5\theta)$. The error field remains smooth and concentrates in the regions where the numerical solution attains its local maxima.

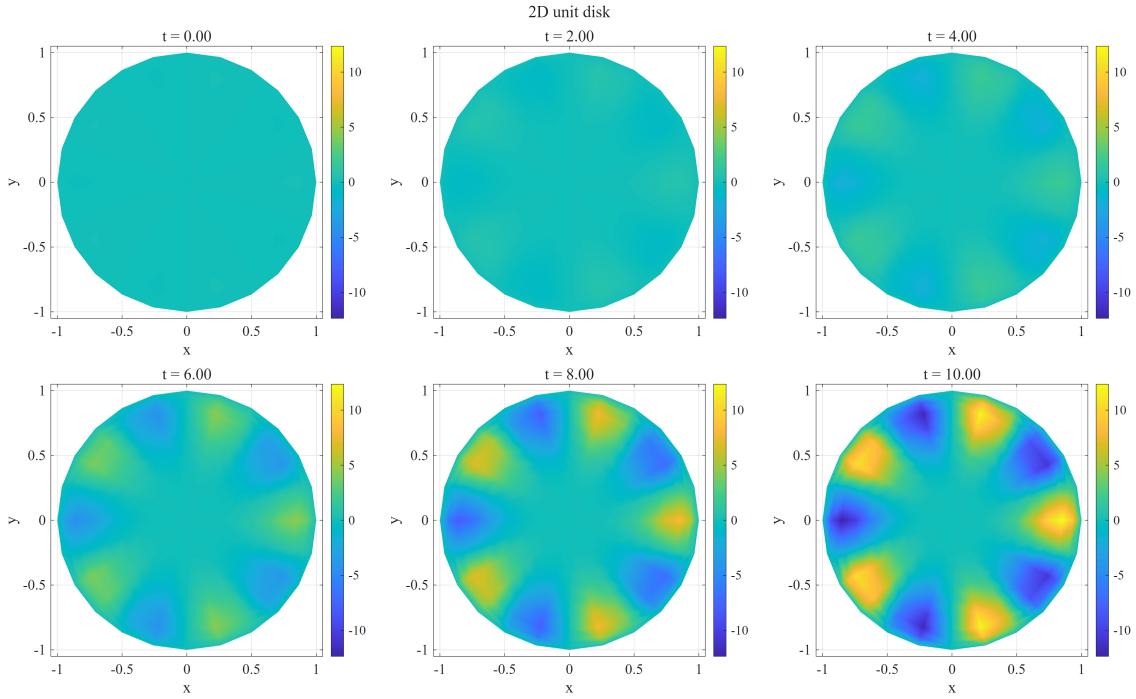


Figure 13: Numerical solution (polar disk): snapshots at $t = 0, 2, 4, 6, 8, 10$.

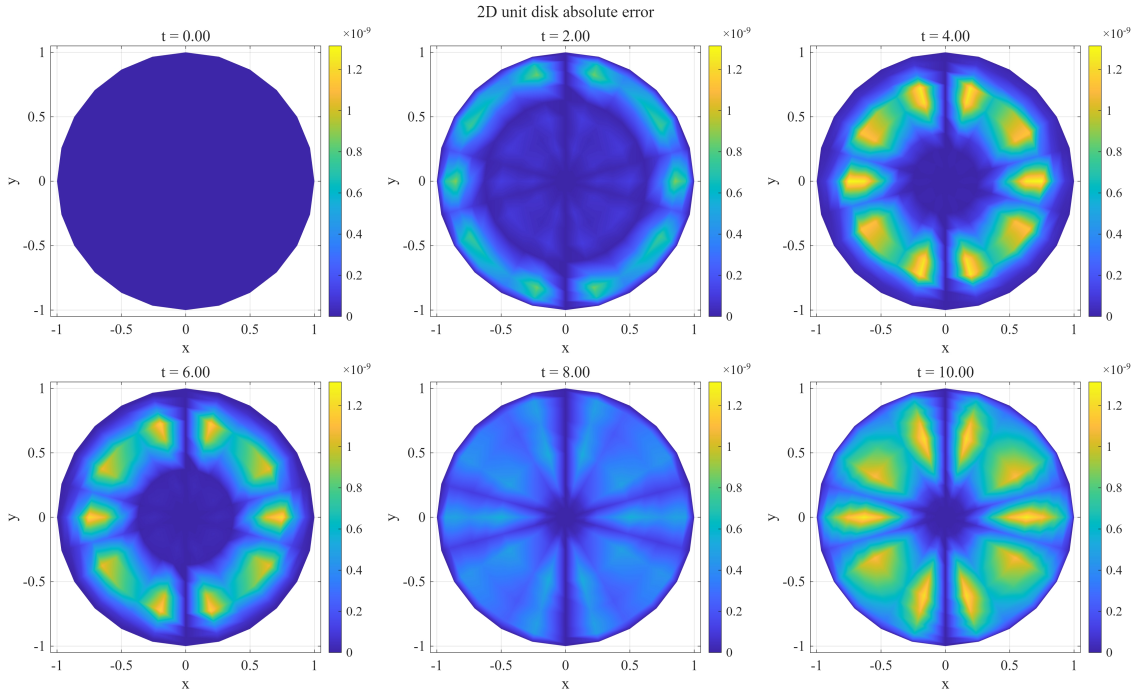


Figure 14: Numerical solution, absolute error $|u_{\text{num}} - u_{\text{exact}}|$, and exact solution (polar disk): snapshots at $t = 0, 2, 4, 6, 8, 10$.

Example 8. We next consider the forced wave equation on the three-dimensional unit ball $\Omega = \{\rho \leq 1\}$ with wave speed $\alpha = 1$. The spatial discretization adopts Chebyshev collocation in the radial direction ρ and the polar angle θ, together with Fourier collocation in the azimuthal angle ϕ, coupled with the second-order

backward differentiation formula (BDF2) for time integration. The manufactured exact solution reads

$$u(\rho,\theta,\phi,t) = \rho^2(1-\rho^2)\sin^2(\theta)\cos(2\phi)\big(1+t^2+\sin t\big), \tag{7.2}$$

and the forcing term is obtained by direct substitution into the wave equation. The initial conditions are

$$u(\rho,\theta,\phi,0) = \rho^2(1-\rho^2)\sin^2(\theta)\cos(2\phi), \quad u_t(\rho,\theta,\phi,0) = \rho^2(1-\rho^2)\sin^2(\theta)\cos(2\phi).$$

Homogeneous Dirichlet boundary conditions are imposed on the spherical boundary $\rho = 1$, and the nonlinear term satisfies $g(u) \equiv 0$. The discretization parameters are $N_\rho = 16$ (17 nodes including endpoints), $N_\theta = 18$ (19 nodes including endpoints), and $N_\phi = 32$, yielding 10336 total degrees of freedom. The simulation runs up to $T = 10.00$ with time step $\tau = 1.0 \times 10^{-4}$, for a total of 10^5 time steps, consuming 12001.70 seconds. Snapshots are recorded at $t = 0, 2, 4, 6, 8, 10$.

Figure 16 and 15 presents snapshots of the numerical solution, the exact manufactured solution, and the corresponding pointwise absolute error at $t = 0, 2, 4, 6, 8, 10$. The solution evolves smoothly in time and retains the angular structure $\sin^2\theta\cos(2\phi)$ of the exact solution. Its amplitude gradually increases as time proceeds, consistent with the temporal factor $1 + t^2 + \sin t$. The final state also reports velocity errors: the L^∞ and RMS errors for the velocity u_t at $t = 10.00$ are 2.5357×10^{-8} and 4.0264×10^{-9}, respectively.

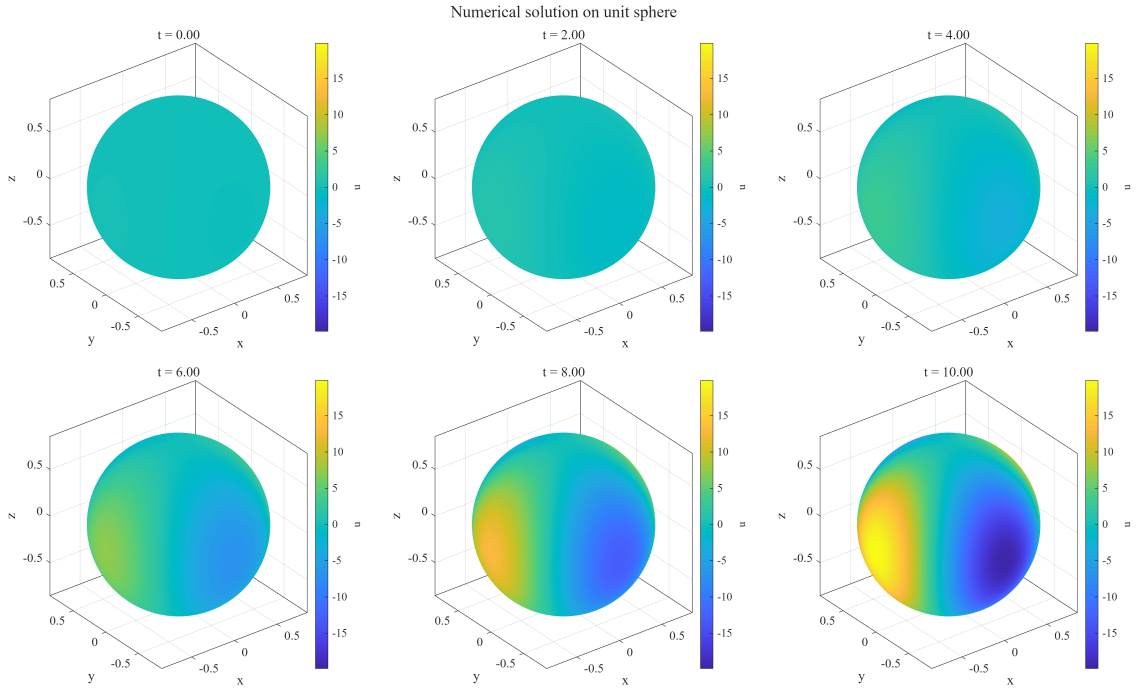


Figure 15: Numerical solution on the unit ball ($\rho \le 1$): snapshots at $t = 0, 2, 4, 6, 8, 10$.

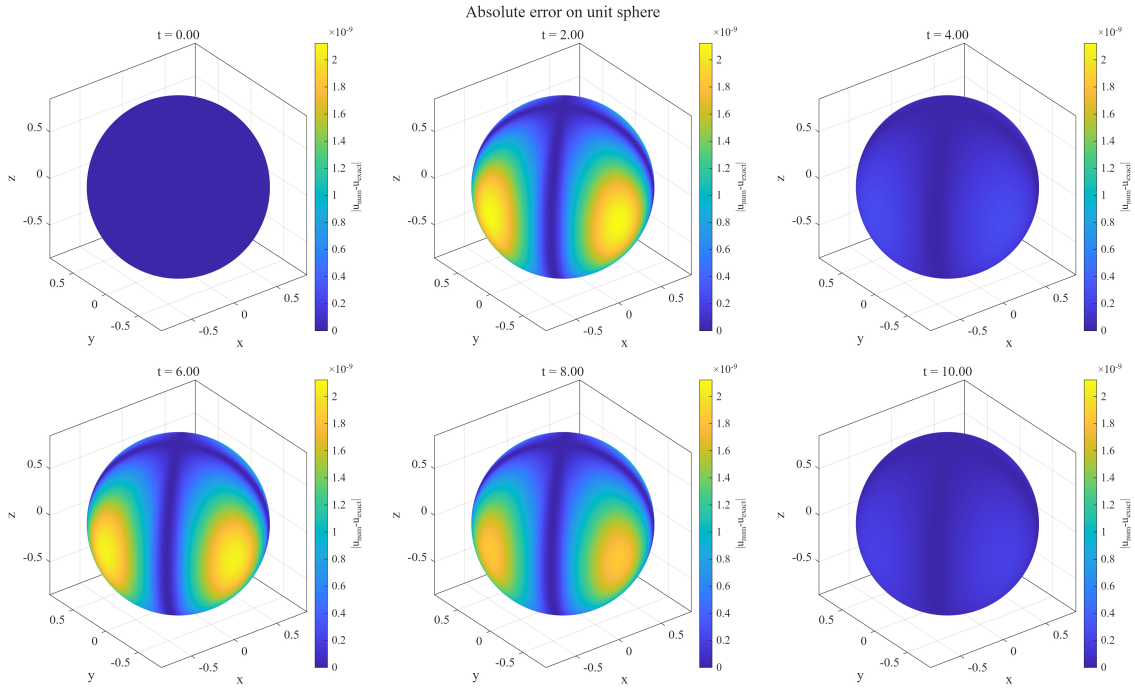


Figure 16: Absolute error $|u_{\text{num}} - u_{\text{exact}}|$ on the unit ball ($\rho \leq 1$): snapshots at $t = 0, 2, 4, 6, 8, 10$.

The L^∞ and RMS errors for the displacement stay around the 10^{-9} level throughout the simulation (Table 10), matching the colour bar whose peak value is approximately 2×10^{-9}. The error field remains smooth and concentrates near the two lobes induced by the $\cos(2\phi)$ angular mode, without visible spurious oscillations. This experiment demonstrates that the spherical spectral collocation solver with BDF2 achieves stable spectral accuracy for the forced wave equation inside the solid unit ball.

Table 10: $\|E(t)\|_{L^2(\Omega)}$ and convergence order at various time instances for different polynomial orders $(N_\rho, N_\theta, N_\phi)$ (forced wave on unit ball, homogeneous Dirichlet boundary, $g(u) \equiv 0$, BDF6)

$(N_\rho, N_\theta, N_\phi)$	Metric	$t = 0.00$	$t = 2.00$	$t = 4.00$	$t = 6.00$	$t = 8.00$	$t = 10.00$
$(8, 9, 16)$	$\|E(t)\|_{L^2(\Omega)}$	0.00×10^{0}	1.07×10^{-5}	7.62×10^{-6}	1.73×10^{-5}	1.03×10^{-5}	9.53×10^{-6}
	order	—	—	—	—	—	—
$(16, 18, 32)$	$\|E(t)\|_{L^2(\Omega)}$	0.00×10^{0}	4.32×10^{-10}	3.08×10^{-10}	6.99×10^{-10}	4.18×10^{-10}	3.88×10^{-10}
	order	0.00	14.62	14.62	14.62	14.62	14.62
$(32, 36, 64)$	$\|E(t)\|_{L^2(\Omega)}$	0.00×10^{0}	1.94×10^{-14}	1.38×10^{-14}	3.14×10^{-14}	1.88×10^{-14}	1.74×10^{-14}
	order	0.00	14.44	14.44	14.44	14.44	14.44

Example 9. We next consider the forced wave equation on a two-dimensional five-petal non-convex domain. The boundary curve is given by $\rho(\theta) = 1 + 0.22\cos(5\theta)$. The spatial discretization uses mapped polar spectral collocation, combined with the BDF2 time integrator. The mesh is 49×48, giving 2352 degrees of freedom. We adopt a fixed time step $\tau = 10^{-4}$, which yields 10^5 time steps to reach the final time $T = 10.00$. The manufactured exact solution reads

$$u(\rho, \theta, t) = \rho^5(1 - \rho^2)\cos(5\theta)\big(1 + t^2 + \sin t\big), \tag{7.3}$$

and the forcing term is obtained by direct substitution into the polar wave operator. The initial conditions are $u(\rho, \theta, 0) = \rho^5(1 - \rho^2)\cos(5\theta)$ and $u_t(\rho, \theta, 0) = \rho^5(1 - \rho^2)\cos(5\theta)$. Homogeneous Dirichlet boundary conditions are imposed, and $g(u) \equiv 0$. Snapshots are recorded at $t = 0, 2, 4, 6, 8, 10$.

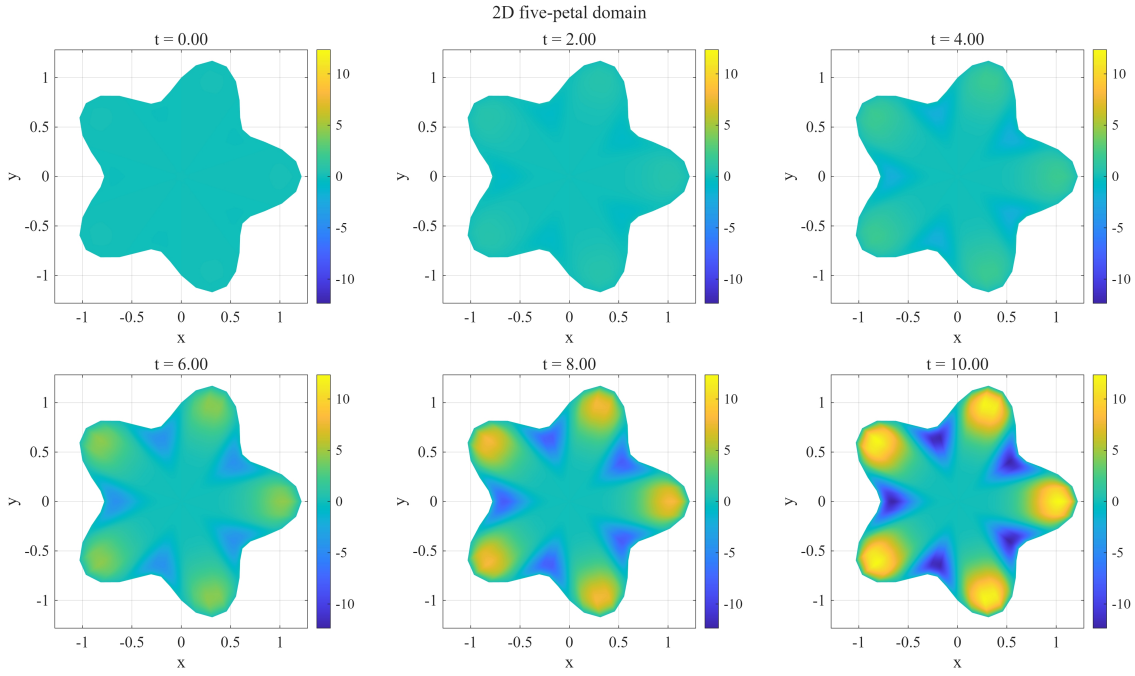


Figure 17: Numerical solution for forced two-dimensional five-petal domain: snapshots at $t = 0, 2.00, 4.00, 6.00, 8.00, 10.00$.

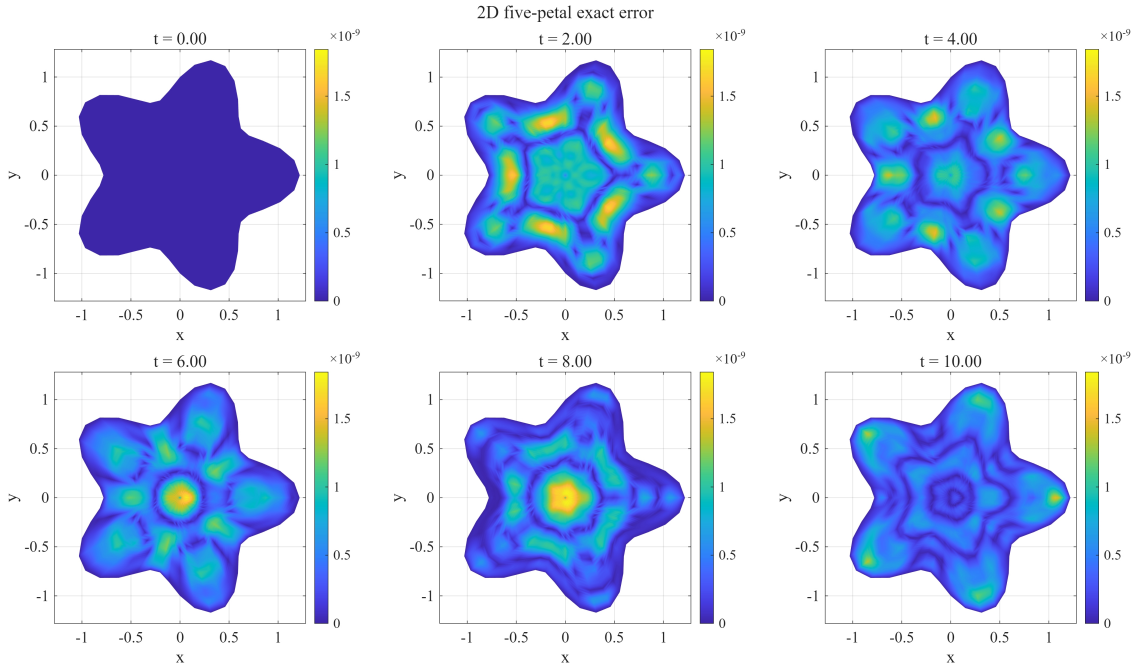


Figure 18: Absolute error $|u_{\text{num}} - u_{\text{exact}}|$ for forced two-dimensional five-petal domain: snapshots at $t = 0, 2.00, 4.00, 6.00, 8.00, 10.00$.

Figure 17 presents snapshots of the numerical solution on the two-dimensional five-petal domain at $t = 0, 2.00, 4.00, 6.00, 8.00, 10.00$. The solution evolves smoothly in time and preserves the five-fold angular structure of the manufactured solution $\cos(5\theta)$. The amplitude grows following the temporal factor $1 + t^2 + \sin t$, with maxima gradually concentrating near the petal tips as time advances.

The corresponding pointwise absolute error $|u_{\text{num}} - u_{\text{exact}}|$ is shown in Figure 18. The error stays uniformly small and distributes smoothly over the deformed petal domain, with its spatial pattern aligned with the five angular lobes of the solution and no visible spurious oscillations or boundary pollution.

Table 11 presents the $\|E(t)\|_{L^2(\Omega)}$ errors and spatial convergence orders for the twodimensional fivepetal forced wave problem with several pairs of radial and angular polynomial degrees (N_ρ, N_θ). The L^2 error decays rapidly as the approximation orders increase, which illustrates the spectral accuracy of the scheme for this multilobe curveddomain test.

Table 11: $\|E(t)\|_{L^2(\Omega)}$ and convergence order at various time instances for different polynomial orders (N_ρ, N_θ) (2D fivepetal forced wave case, BDF6)

(N_ρ, N_θ)	Metric	$t = 0.00$	$t = 2.00$	$t = 4.00$	$t = 6.00$	$t = 8.00$	$t = 10.00$
$(25, 24)$	$\|E(t)\|_{L^2(\Omega)}$	0.00×10^{0}	1.79×10^{-5}	1.56×10^{-5}	1.96×10^{-5}	2.21×10^{-5}	8.46×10^{-6}
	order	—	—	—	—	—	—
$(49, 48)$	$\|E(t)\|_{L^2(\Omega)}$	0.00×10^{0}	7.31×10^{-10}	6.37×10^{-10}	8.00×10^{-10}	9.01×10^{-10}	3.45×10^{-10}
	order	0.00	14.58	14.58	14.58	14.58	14.58
$(97, 96)$	$\|E(t)\|_{L^2(\Omega)}$	0.00×10^{0}	3.26×10^{-14}	2.84×10^{-14}	3.57×10^{-14}	4.02×10^{-14}	1.54×10^{-14}
	order	0.00	14.49	14.49	14.49	14.49	14.49

Example 10. We next consider the forced wave equation on a three-dimensional five-petal rose domain. The boundary surface reads $\rho(\theta, \phi) = 1+0.25 \sin^2\theta \cos(5\phi)$. The spatial discretization uses mapped spherical spectral collocation with a grid of $13 \times 17 \times 16$ (radial $\times$ polar $\times$ azimuthal), combined with the BDF2 time integrator. The manufactured exact solution reads

$$u(\rho, \theta, \phi, t) = \rho^2(1 - \rho^2) \sin^2\theta \cos(2\phi)\big(1 + t^2 + \sin t\big), \tag{7.4}$$

and the forcing term is obtained by direct substitution into the spherical wave operator. The initial conditions are $u(\rho, \theta, \phi, 0) = \rho^2(1-\rho^2) \sin^2\theta \cos(2\phi)$ and $u_t(\rho, \theta, \phi, 0) = \rho^2(1-\rho^2) \sin^2\theta \cos(2\phi)$. Homogeneous Dirichlet boundary conditions are imposed, and $g(u) \equiv 0$. The simulation runs up to $T = 1.00$, with snapshots recorded at $t = 0, 0.2, 0.4, 0.6, 0.8, 1.0$, and the fields are sampled on the surface $\rho \approx 0.933$.

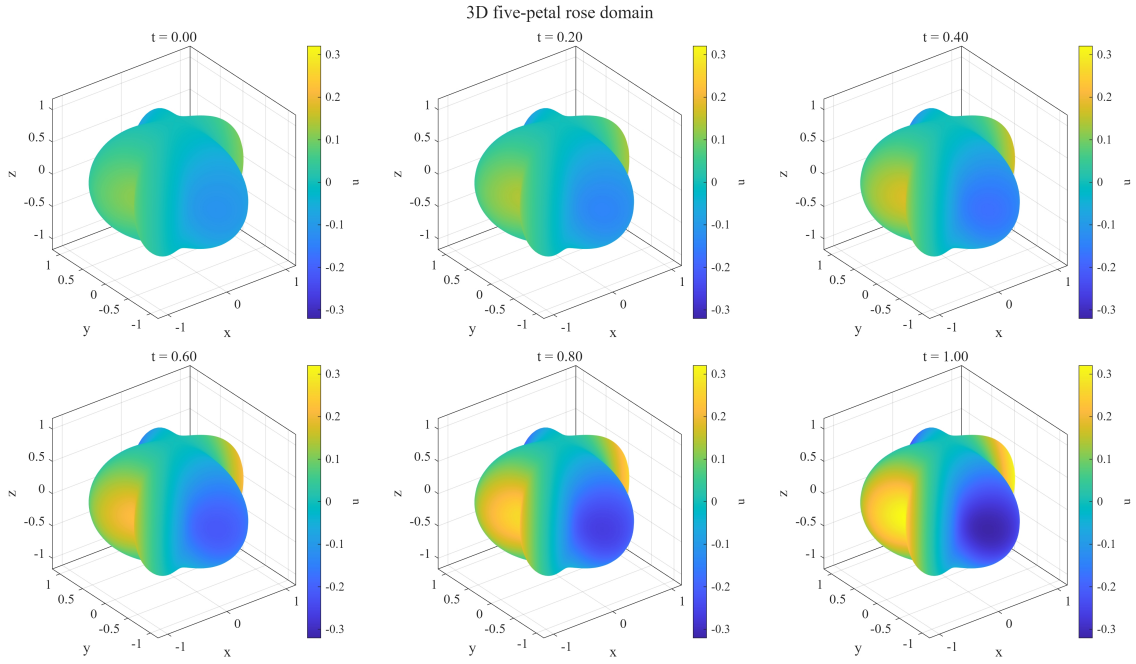


Figure 19: Numerical solution for forced three-dimensional five-petal rose domain, sampled at $\rho \approx 0.933$: snapshots at $t = 0, 0.20, 0.40, 0.60, 0.80, 1.00$.

Figure 19 presents snapshots of the numerical solution on the three-dimensional five-petal rose domain at $\rho \approx 0.933$ for $t = 0, 0.20, 0.40, 0.60, 0.80, 1.00$. The solution evolves smoothly in time and preserves the angular structure of the manufactured solution $\sin^2\theta\cos(2\phi)$. The amplitude evolves consistently with the temporal factor $1 + t^2 + \sin t$, and no noticeable boundary pollution is observed on the deformed rose boundary.

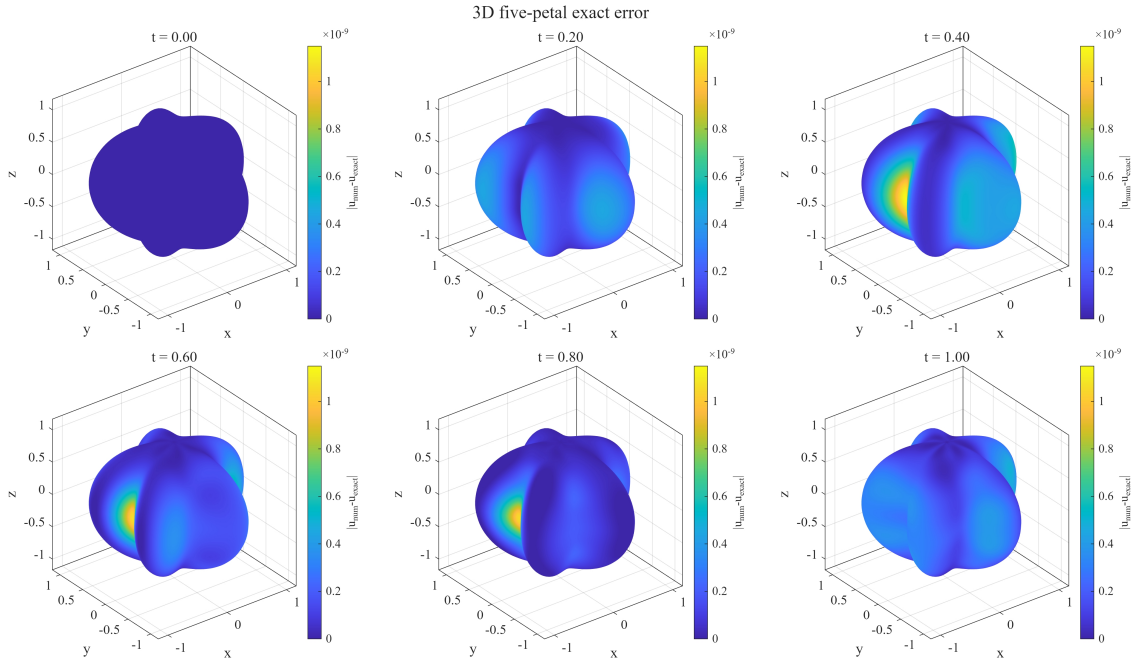


Figure 20: Absolute error $|u_{\text{num}} - u_{\text{exact}}|$ for forced three-dimensional five-petal rose domain, sampled at $\rho \approx 0.933$: snapshots at $t = 0, 0.20, 0.40, 0.60, 0.80, 1.00$.

The corresponding pointwise absolute error $|u_{\text{num}} - u_{\text{exact}}|$ is shown in Figure 20. The error stays at a low level and distributes smoothly over the curved rose surface, with its spatial pattern aligned with the angular lobes of the solution and no visible spurious oscillations.

The L^∞ and RMS errors remain at the order of 10^{-9} throughout the simulation (Table 12), which is consistent with spectral accuracy for smooth manufactured solutions. The error distribution is smooth and follows the angular mode structure of the exact solution. This test validates the mapped spherical spectral solver on fully non-axisymmetric, deformed three-dimensional curved domains.

Table 12: $\|E(t)\|_{L^2(\Omega)}$ and convergence order at various time instances for different polynomial orders $(N_\rho, N_\theta, N_\phi)$ (3D fivepetal rose forced wave case, BDF6)

$(N_\rho, N_\theta, N_\phi)$	Metric	$t = 0.00$	$t = 0.20$	$t = 0.40$	$t = 0.60$	$t = 0.80$	$t = 1.00$
$(7, 9, 8)$	$\|E(t)\|_{L^2(\Omega)}$	0.00×10^{0}	5.89×10^{-6}	1.37×10^{-5}	2.10×10^{-5}	2.10×10^{-5}	5.19×10^{-5}
	order	—	—	—	—	—	—
$(13, 17, 16)$	$\|E(t)\|_{L^2(\Omega)}$	0.00×10^{0}	2.38×10^{-10}	5.54×10^{-10}	8.49×10^{-10}	8.49×10^{-10}	2.10×10^{-9}
	order	0.00	14.60	14.60	14.60	14.60	14.60
$(25, 33, 32)$	$\|E(t)\|_{L^2(\Omega)}$	0.00×10^{0}	1.06×10^{-14}	2.47×10^{-14}	3.79×10^{-14}	3.79×10^{-14}	9.38×10^{-14}
	order	0.00	14.46	14.46	14.46	14.46	14.46

8. Conclusion

This work, we develop the LegendreGalerkin Chebyshevcollocation sixthorder backward differentiation formula (LCCBDF6) scheme for longtime numerical simulation of multidimensional linear wave equations defined on complex geometric domains. The spatial discretization combines LegendreGalerkin variational formulation with Chebyshev collocation on GaussLobatto nodes, while the sixthorder multistep BDF6 method is adopted for temporal discretization. To initialize the sixstep BDF recursion, a sequential startup strategy using loworder BDF schemes with identical spatial spectral discretization is constructed to supply the required initial multistep solution layers.

We carry out a rigorous stability and convergence analysis for the fullydiscrete LCCBDF6 scheme. By modal decomposition based on the generalized eigenvalue problem of the spatial operator, we derive a CFLtype conditional stability constraint for BDF6, which restricts the product of wave speed, time step and the squareroot of maximum spatial eigenvalue. Under this stability condition, uniform stability estimates independent of total simulation time steps are established. Further, optimal error bounds are proven: the numerical solution achieves $\mathcal{O}(\tau^6+N^{1-\sigma})$ accuracy in the H^1-norm for displacement and L^2-norm for velocity, where τ denotes timestep size, N is polynomial degree and σ represents solution regularity. Longtime error analysis indicates that the error grows at most linearly with simulation time, which originates mainly from phase error accumulation for oscillatory wave solutions.

Via appropriate coordinate transformation techniques, the proposed spectral framework is extended to curved nontensorproduct domains, including unit disk, solid sphere, starshaped fivepetal planar domain and threedimensional roselike deformed domain. Singular terms arising from polar and spherical coordinate mappings are treated by algebraic regularization, and Dirichlet boundary constraints are enforced by modifying corresponding rows of the discrete system matrix.

Numerical experiments are implemented for one, two and threedimensional wave problems on rectangular, circular, spherical and irregular starshaped geometries, covering both homogeneous sourcefree cases and forced problems with manufactured analytical solutions. The numerical results validate the theoretical convergence order and conditional stability property. The method maintains spectral accuracy throughout longtime integration; pointwise L^∞ and rootmeansquare errors stay at magnitude around 10^{-9} for curveddomain test examples, without obvious spurious oscillations or boundary pollution.

Nevertheless, the BDF6 scheme is not Astable, so the time step is subject to stability restriction $\tau = \mathcal{O}(N^{-2})$. In future research, the KosloffTalEzer mapping can be introduced to relax this stepsize constraint. Moreover, the present framework can be generalized to nonlinear wave equations, variablecoefficient wave problems and more complicated multicomponent physical models on arbitrary curved domains.

Author contribution

Qiancheng Tan: Methodology, Implementation, Software, Data curation, Visualization, WritingOriginal draft preparation, WritingReviewing and Editing.
Yonghui Qin: Conceptualization, Methodology, Supervision, Funding acquisition, WritingReviewing and Editing.

Funding

This work was supported by the National Natural Science Foundation of China (No.12561067 and No.12161025), the Science and Technology Project of Guangxi (No.GuikeAD25069086), and the Guangxi Key Laboratory of Automatic Detecting Technology and Instruments (YQ22106).

Declarations

Conflict of interest

The authors declare no competing interests.

Data Availability

All data generated or analysed during this study are included in this published article and its supplementary information files.

References

[1] Georgios Akrivis and Emmanouil Katsoprinakis. Maximum angles of $a(\vartheta)$-stability of backward difference formulae. *BIT Numerical Mathematics*, 60(1):93–99, 2020.

[2] Z. Aldirany, R. Cottereau, M. Laforest, and S. Prudhomme. Optimal error analysis of the spectral element method for the 2d homogeneous wave equation. *Computers & Mathematics with Applications*, 119:241–256, 2022.

[3] Uri M Ascher and Linda R Petzold. *Computer Methods for Ordinary Differential Equations and Differential-Algebraic Equations*. SIAM, 1998.

[4] John P Boyd. *Chebyshev and Fourier Spectral Methods*. Dover Publications, 2001.

[5] Claudio Canuto, M Yousuff Hussaini, Alfio Quarteroni, and Thomas A Zang. *Spectral Methods: Fundamentals in Single Domains*. Springer Science & Business Media, 2006.

[6] Y. Cao, B. Li, and Z. Zhang. Energypreserving spectral galerkin methods for secondorder wave equations. *Journal of Scientific Computing*, 88(3):Paper No. 54, 26, 2021.

[7] David Cohen, Ernst Hairer, and Christian Lubich. Modulated fourier expansions for multistep methods applied to highly oscillatory ordinary differential equations. *Foundations of Computational Mathematics*, 5(3):261–287, 2005.

[8] David Cohen, Ernst Hairer, and Christian Lubich. Longtime analysis of numerical integrators for wave equations via modulated fourier expansions. *Mathematics of Computation*, 77(263):1447–1473, 2008.

[9] Benjamin Dörich and Jan Leibold. Full discretization error analysis of exponential integrators for semilinear wave equations. *Mathematics of Computation*, 91(336):1687–1709, 2022.

[10] Bengt Fornberg. A classroom note on calculation of polar singularities in pseudospectral methods. *SIAM Review*, 40(3):685–692, 1998.

[11] David Gottlieb and Jan S Hesthaven. Spectral methods for time-dependent problems. *Journal of Computational and Applied Mathematics*, 128(1-2):83–165, 2001.

[12] David Gottlieb and Steven A Orszag. *Numerical Analysis of Spectral Methods: Theory and Applications*. SIAM, 1977.

[13] Ernst Hairer and Christian Lubich. Longtime error analysis of linear multistep methods for oscillatory differential equations. *BIT Numerical Mathematics*, 40(4):668–682, 2000.

[14] Ernst Hairer, Christian Lubich, and Gerhard Wanner. *Geometric Numerical Integration: Structure-Preserving Algorithms for Ordinary Differential Equations*. Springer Science & Business Media, 2006.

[15] Jan S Hesthaven and Tim Warburton. *Nodal Discontinuous Galerkin Methods: Algorithms, Analysis, and Applications*. Springer Science & Business Media, 2007.

[16] A. R. Humphries and A. M. Stuart. Uniform bounds for dissipative dynamical systems and their discretizations. *SIAM Journal on Numerical Analysis*, 31(6):1672–1694, 1994.

[17] Jie Shen. Efficient spectral-galerkin methods iii: Polar and spherical geometries. *SIAM Journal on Scientific Computing*, 25(2):525–539, 2003.

[18] Jie Shen, Tao Tang, and Li-Lian Wang. *Spectral Methods: Algorithms, Analysis and Applications*, volume 41. Springer Science & Business Media, 2011.

[19] Lloyd N Trefethen. *Spectral Methods in MATLAB*. SIAM, 2000.

[20] P. J. van der Houwen. Longterm behaviour of multistep methods for oscillatory differential equations. *SIAM Journal on Numerical Analysis*, 26(6):1576–1589, 1989.